THE UNIVERSITY OF OKLAHOMA

GRADUATE COLLEGE

DRAG CHARACTERISTICS FOR A COMPLIANT SURFACE AIRFOIL

A DISSERTATION

SUBMITTED TO THE GRADUATE COLLEGE

in partial fulfillment of the requirements for the

degree of

DOCTOR OF PHILOSOPHY

By

HUMPHREY H. CHU

Norman, Oklahoma

1971

DRAG CHARACTERISTICS FOR COMPLIANT

SURFACE AIRFOIL

APPROVED BY

Edward J. Blasta

Raymond Kaser

William N. Hughes

DISSERTATION COMMITTEE

ACKNOWLEDGMENT

The work reported herein is part of a project supported by funds from the U.S. Army (ARO-D Project No. 5596-E under contract no. DA-31-124-ARO-D-349), and was conducted at the Aerospace and Mechanical Engineering Laboratory located on the Research Park of the University of Oklahoma.

The author would like to express his gratitude to Dr. E.F. Blick for his encouragement, inspiration and guidance during this study and throughout the graduate program. Also, the time and effort of Dr. R.V. Kaser, Dr. D.M. Egle and Dr. W.N. Huff have been sincerely appreciated.

Special thanks also goes to Mr. Phil Crenshaw for his help to operate tunnels for the experiments.

Finally, I would like to dedicate this dissertation to the memory of my late dear father, Mr. C.L. Chu.

ABSTRACT

As part of a program to investigate the feasibility of reducing aerodynamic skin-friction drag by the use of compliant coatings, a detailed wind-tunnel study was made to determine the drag characteristics of a compliant coating on an airfoil. The compliant surface was constructed with different thickness (0.001 to 0.025 inch) of polyvinyl-chloride (PVC) membrane backed by a 3/16 to 6/16 inch damping layer of polyurethane foam (40 PPI). The foam was bonded to specially designed airfoils to form NACA 0009 airfoils. Hard surface NACA 0009 airfoils were also constructed. A reduction of skin friction drag was recorded. To be sure the drag reduction did not come from the shifting of the transition line, both experimental (china-clay) and theoretical (von-Karman-Pohlhausen) methods were used to determine the transition point.

TABLE OF CONTENTS

LIST OF TABLES

LIST OF FIGURES

NOMENCLATURE

A	airfoil projected area
A_1, A_2	cross section area of tunnel at entrance and test section
C	airfoil chord line
C_f	skin friction drag coefficient
C_{DC}	correction for wing tip drag coefficient
C_D	drag coefficient
$F(K), f_1(K)$	universal function for the calculation of compressible laminar boundary layers
h_{lost}	head loss
K	$K = \Lambda\ (\theta/\sigma)^2$
K_1	head/q_2
K_2	$(A_2/A_1)^2$
K_3	$(P_1-P_2)/q_2$
K_4	$V_2[\rho/(P_1-P_2)]^{\frac{1}{2}}$
L	lift force
ℓ	airfoil chord length
P_1, P_2	static pressure at entrance and test section of the tunnel
q_1, q_2	dynamic head = $\frac{1}{2}\ \rho V_{1,2}^2$
R	resultant aerodynamic force
s	arc length measured from the stagnation point along the wetted surface

t^*	PVC skin thickness
t	airfoil thickness
U_o, V_o	free stream velocity
U_m	non-dimensional velocity in potential flow
U	local velocity
α	angle of attack
ϵ	down wash angle
σ^*	boundary layer displacement thickness
Λ	shape factor of laminar boundary layer velocity profile
ν	kinematic viscosity
τ_o	shearing stress at wall
τ	perturbation Reynold stress
θ	boundary layer momentum thickness
ρ	density of air
ω	frequency of the exitation pressure

DRAG CHARACTERISTICS FOR COMPLIANT SURFACE AIRFOIL

CHAPTER I

INTRODUCTION

Dynamic Forces on a Body Immersed in a Fluid

The motion of a body immersed in a fluid is related to the drag and lift components of the resultant dynamic forces. These forces are caused by two factors. First, shear stresses, due to viscosity and velocity gradients at the boundary surface, cause forces tangential to the surface. Second, pressure intensities which vary along the surface due to dynamic effects result in forces normal to the boundary. For an immersed body, the vector sum of the normal and tangential surface forces integrated over the complete surface gives a resultant force vector, as illustrated in Figure 1-1. The

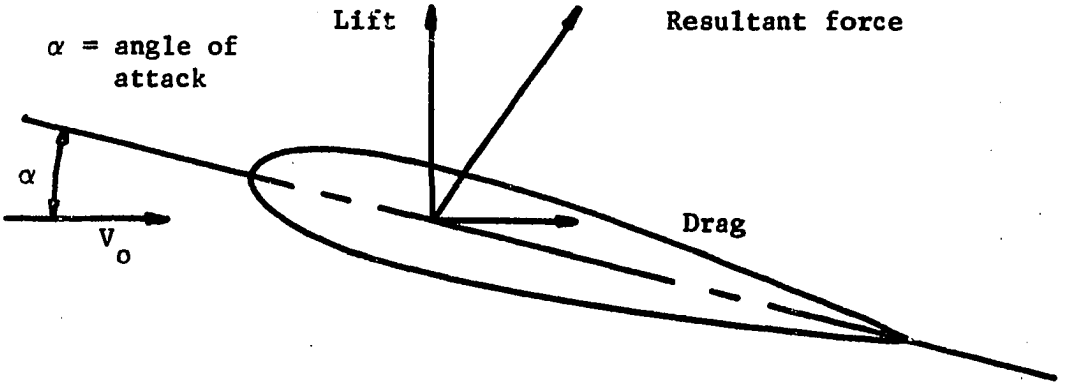

Figure 1-1. Lift and drag on a body immersed in a fluid

component of this resultant force in the direction of the relative velocity V_o ahead of the body is the drag D. The component normal to the relative velocity is the lift force L. Both drag and lift include frictional and pressure components, but the frictional component of lift is extremely small. The frictional drag is also known as surface resistance or skin friction drag. The pressure drag has its origin in two phenomena. One is related to the lift of the body and the other is related to the size and form or shape of the body. The former is known as induced drag, the latter as form or wake drag. It is obvious lifting bodies have induced drag while non-lifting bodies have no induced drag. (Figure 1-2).

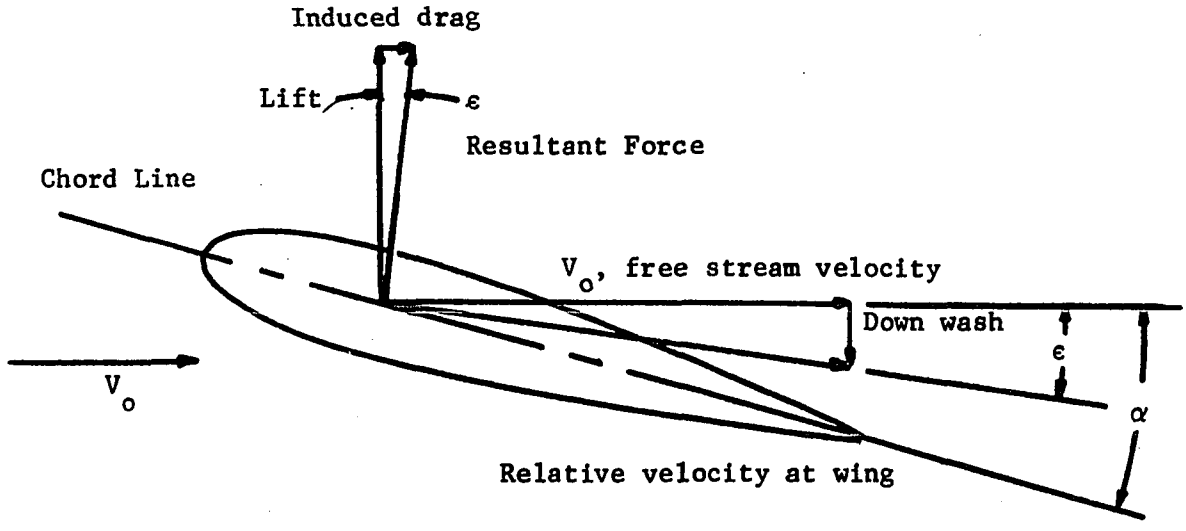

Figure 1-2. Induced drag on a wing

Skin-friction drag is caused duly by the viscosity of fluid. The effects of viscosity are of primary importance in a thin region near the surface of the wing called the "boundary layer". Boundary layers, in general, are of two types, namely, laminar boundary

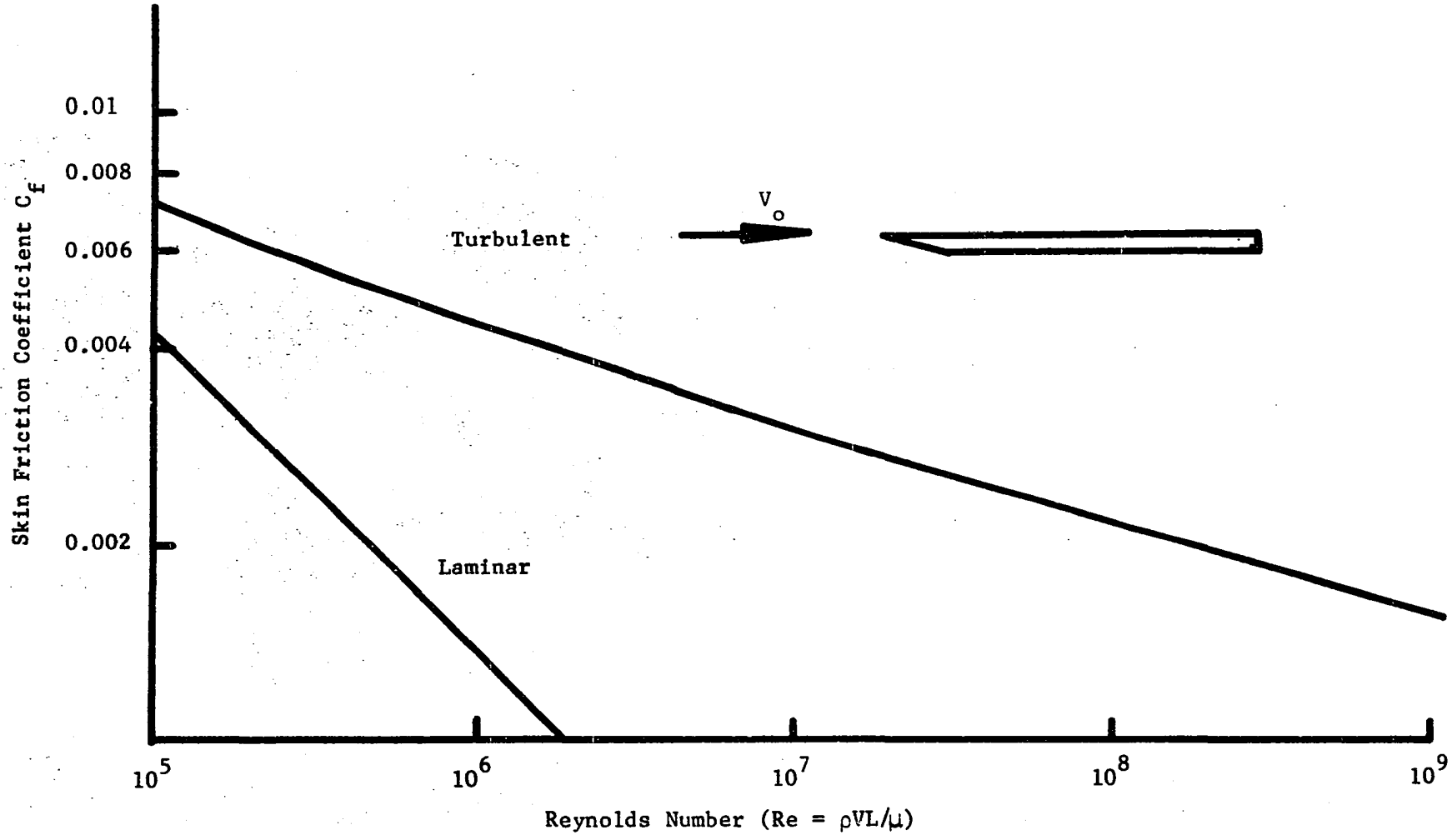

Figure (1-3). The Effect of turbulent and Laminar Flow on the Skin Friction Coefficient for Flat Plates

layer and turbulent boundary layer. The flow in the laminary boundary layer is smooth and free from any eddying motion. The flow in the turbulent boundary layer is characterized by the presence of a large number of relatively small eddies. The eddies in the turbulent boundary layer produce a transfer of momentum from the relatively faster moving outer parts of the boundary layer to the portions closer to the surface. Consequently, the distribution of average velocity is characterized by relatively higher velocities near the surface and a greater total boundary layer thickness than a laminar boundary layer developed under otherwise identical conditions. Skin-friction drag force is, therefore, higher for turbulent boundary layer flow than for laminar flow. (Figure 1-3). When the pressures along the body surfaces are increasing in the direction of flow, deceleration takes place. The relative loss of speed is greater for the particles of fluid within the boundary layer than for those at the outer limits of the layer, because the reduced kinetic energy of the boundary-layer air limits its ability to flow against the adverse pressure gradient. If the rise in pressure is sufficiently great, portions of the fluid within the boundary layer may actually have their direction of motion reversed and may start moving upstream. When this reversal occurs, the boundary layer is said to be "separated". As a result of the increased interchange of momentum from different parts of the layer, turbulent boundary layers are much more resistant to separation than laminar layers. (Figure 1-4). The separation of the boundary layer generates a wake which causes a great wake drag. Artillery shells have sharply truncated tails

(Figure 1-5), and have a large wake with a corresponding large wake drag. The wake drag can be reduced by careful shaping of the body so that the flow follows the body contour almost to the trailing edge of the body. Hence, separation of the flow can be delayed or eliminated. This shaping of a body to reduce the wake drag is called streamlining. Modern airfoils are well streamlined, and consequently have very small wake drag.

Reduction of Drag

Since drag is the main factor for fuel consumption in level flight, it is only logical for man to seek every possible way to reduce drag. Streamlining has reduced wake drag as discussed in the

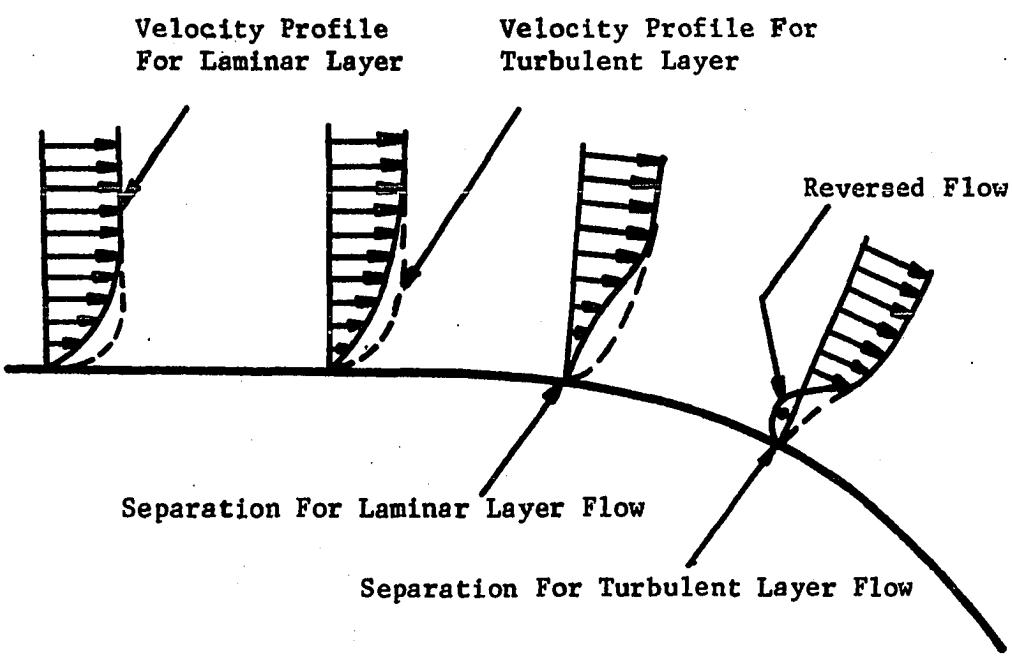

Figure 1-4. Flow Past A Curved Surface

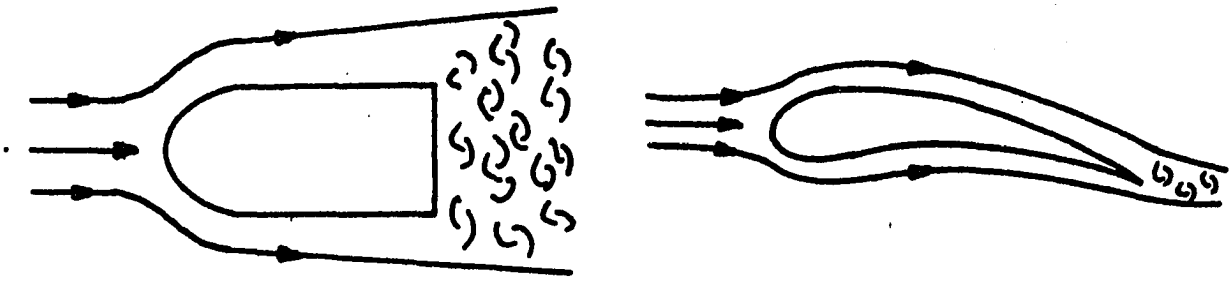

Artillery Shell-Large Wake Drag Airfoil-Small Wake Drag

Figure 1-5. Wake Drag

previous section.

Laminar flow has much less skin-friction than turbulent flow. Smooth skin construction and/or sucking away of the slower velocity particles (causing the boundary layer to be thinner) can delay the transition of the laminar boundary layer to a turbulent boundary layer. In addition, sucking the boundary layer can avoid early flow separation. The saving in drag varies from sixty-five to eighty-five percent in a range of Reynold's number $R = 10^6$ to 10^8 (1) on flat plate at zero incidence with suction maintaining laminar flow at optimum suction . There is a penalty to be paid however, in increased weight and the complexity of the airplane due to the pumps and plumbing.

Kramer (2,3,4), discovered a new method of drag reduction in 1957. Inspired by dolphin's skin, he constructed a body which had what he considered to be the three basic components of the dolphin's skin:

(1) The smooth pressure sensitive diaphram.

(2) The structure supporting the diaphram.

(3) The damping fluid beneath the diaphram.

He measured a reduction in drag of up to fifty percent at a Reynold's number of 1.5×10^7. Following his footstep, Maestrello (5), Ritter & Messum (6), Pelt (7), Karplus (8), Benjam (9), Gregory and Love (10), tried both theoretical and experimental methods to further investigate the possibility of drag reduction contributed by a compliant coating which is the simulation of a dolphin's skin.

Here at the University of Oklahoma, under the direction of Dr. E.F. Blick (11, 12, 13, 14, 15, 16, 17), further tests were conducted on a compliant skin flat plate in wind tunnels. The compliant coating were constructed by using Polyvinyl chloride skin (thickness ranging from .0025 to .0035 inches) stretched over various damping fluids as shown in Figure (1-6). Tests were also run using polyurethane foam instead of the damping fluids. Results of these tests are shown in Table (1.1) (17). (Figure 1-7) shows a graph of skin friction coefficient versus Reynold's number for the compliant coating (13).

The success of compliant coating flat plate tests led the author to investigate the possibility of drag reductionfor airfoils covered with compliant coatings.

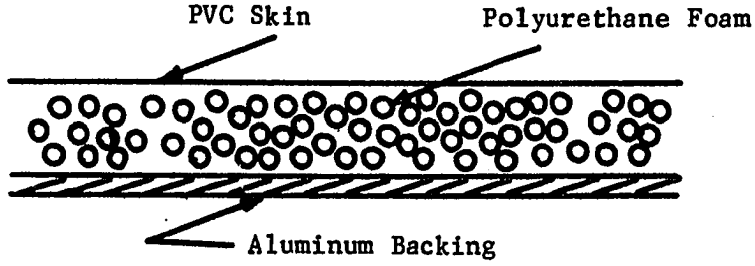

Figure 1-6. Compliant Skin Coating

Table 1.1. Turbulent Skin Friction Coefficients* (17) at 38 fps

Material	Bare	PVC Skin	PVC Skin and Wet
Hard Surface	0.0043	--	--
27 PPI	0.0129	0.0044	0.0030
40 PPI	0.0089	0.0032	0.0027
80 PPI	0.0074	0.0029	0.0034
Foam Rubber	0.0054	0.0074	0.0084

* C_F = (skin friction)/(area) (dynamic pressure)

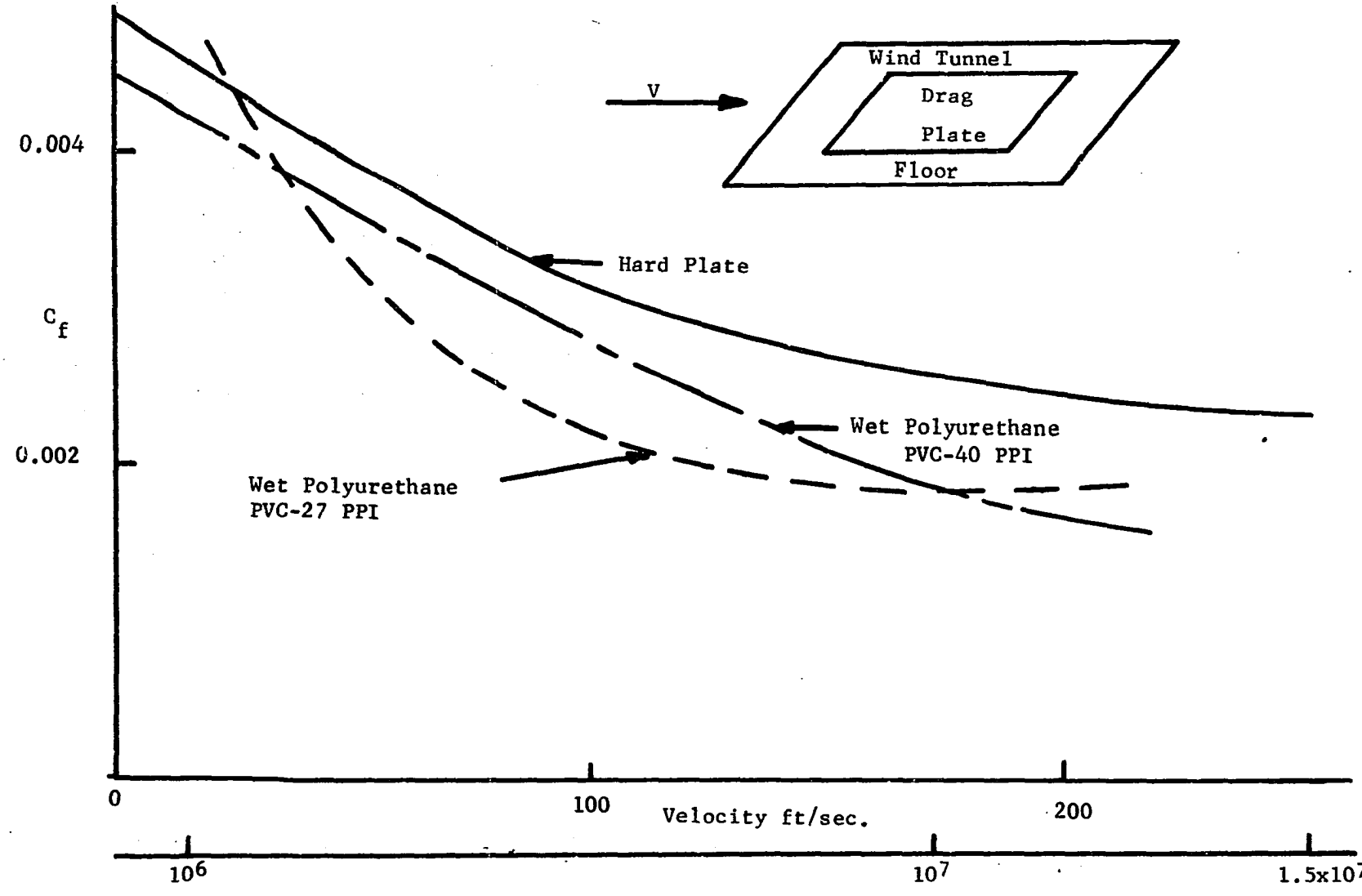

Figure 1-7 Compliant Coating Drag Reduction (16)

CHAPTER II

WIND TUNNEL TEST FACILITIES

TUNNEL I

Entrance Section

Tunnel I was an open-circuit tunnel. The entrance bellmouth of the tunnel was designed to provide a minimum of turbulence in the test section main stream flow by attaching a pre-contraction box incorporating two layers of number sixteen size fiberglass screens one foot apart and three inches of thin aluminum honeycomb with three-eighth inch cell size. The tunnel has a 16:1 contraction ratio. (Figure 2-1). It can be noted from Uberio's (18), work, this particular contraction ratio gave a favorable decrease in the longitudinal component of turbulence without too large an increase in the lateral component.

The contraction, as shown in figure 2-1 was fabricated from two steel rings, five feet and one and one-half feet in diameter, and the wall was made of fiberglass and epoxy. A two and one-half foot long pre-contraction settling chamber was used with a five foot post-contraction length. The settling chamber allows time for honeycomb and screen flow disturbances to dampen considerably before entering

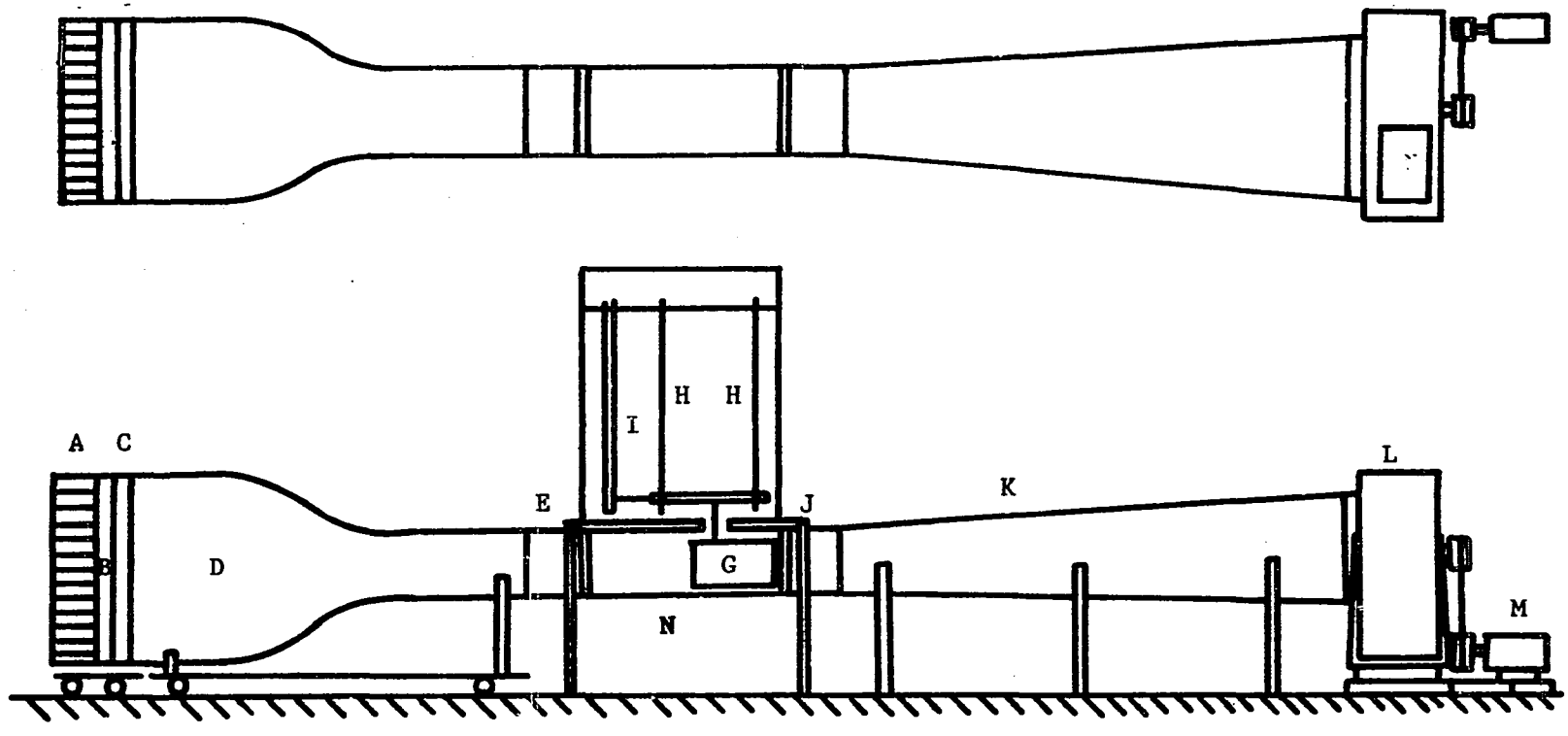

A. Honey Comb
B. Settling Chamber
C. Screens
D. Entrance Bellmouth
E. Round to Rectangular Converter
F. Floating Steel Plate
G. Model Airfoil
H. Suspension Cables
I. Aluminum Column
J. Rectangular to Round Converter
K. Diffuser
L. Centrifugal Fan
M. Driving Motor
N. Test Section

Figure 2-1. Schematic of Tunnel 1

the contraction. The three foot post-contraction length helped to provide a fully developed parallel flow before reaching the test section. A three inch deep, three-eighth inch cell size aluminum honeycomb was fastened in a three-quarter inch thick plywood frame such that the trailing edge of the honeycomb was six inches in front of the first fiberglass screen. The second fiberglass screen was one foot from the first screen. These screens were made of number sixteen size fiberglass screen. This arrangement cut down the wake size and helped to provide proper alignment of air flow. A foot and one-half long round-to-rectangular converter section (EJ Figure 2.1) was fixed to the aft-end of the post-contraction part of the entrance section and bolted to the test section.

The Diffuser

Since the power loss in a wind tunnel varies with the cube of the air speed, it was desirable to increase the cross-sectional area of diffuser before the airstream reached the driving unit and hence reduced the local tunnel speed as rapidly as possible. The rate of this area increase was limited by the amount of expansion the air would stand without separating from the wall with accompanying large losses. The total angle of expansion for the diffuser was seven degrees which resulted in satisfactory performance.

The Power Train

A Fan, built by ILG Electric Ventilating Co. (BBS 4450) was installed. This fan had a wheel diameter of 20 inches, a fan outlet

area of 12 square feet, and an inlet diameter of 48 inches. This fan was set on four three-quarter inch diameter threaded rods welded to a steel channel and I-beam frame. Also, on this frame was attached a 1770 rpm thirty horsepower electric motor for the power source of the drive unit which was isolated from the test room by medium-hard rubber disks about an inch thick and one and one-half inch diameter. The fan was fixed at 550 rpm. According to the fan specifications at 550 rpm, it would deliver approximately 16,000 cfm. A variable inlet vane was installed between the end of the diffuser and the inlet of the fan. The vanes could be adjusted by a hydraulic cylinder controllable by a hand pump located near the test section. Thus, these vanes regulated the free stream velocity at the test section. The speed range of this tunnel at the test section was fifteen to two hundred eighty feet per second. A one and one-half foot rectangular-to-round converter section, similar to the round-to-rectangular converter section mentioned before, was fixed on the entrance of the diffuser and bolted to the rear part of the test section.

The Test Section

The test section was made of plywood with two by two inch solid wood frames. The test section was supported by screen adjustments attached to two A-frame structures anchored to the floor. The interior walls were finished with sanding, lacquer finishes and a coat of plastic varnish to give an aerodynamically smooth surface. The dimensions of the test section were four feet long, eighteen inches

deep, and thirteen inches high. There were two twenty inch by nine inch windows, one on either side of the test section. The windows were constructed of one-eighth inch thick plexiglass enclosed in aluminum frames.

Balance System

A plywood box of three feet high, two feet deep, three feet wide with a two and one-half feet wide, one-half foot high plexiglass window at the lower front face and a two feet by two feet plywood door above the window, was placed on top of the test section. (Figure 2-2). This box was used to house the balance system. Vibration could pre-maturely cause transition from a laminar to a turbulent boundary layer, thus it was necessary to isolate the balance system box from fan vibration. The box was supported by two A-frames. A one and one-half inch by three inch rectangular steel channel joining the balance system box and the test section was cushioned with a six inch diameter one-eighth inch thick rubber diaphragm to minimize translation of vibration from test section to balance system.

The primary interest of this experiment was to measure skin-friction drag. To ensure a zero induced drag, zero lift was maintained throughout the test. A balance system capable of measuring drag and lift forces was essential. After studying different types of balance systems, a cable-suspended-floating-plate-balance system was chosen. This system was relatively easy to build and met the requirements mentioned above. A steel plate of thirteen by eight

A. Door

B. Hinges

C. Clamps

D. Windows

E. Hand Pumps

F. Switches

G. Test Section

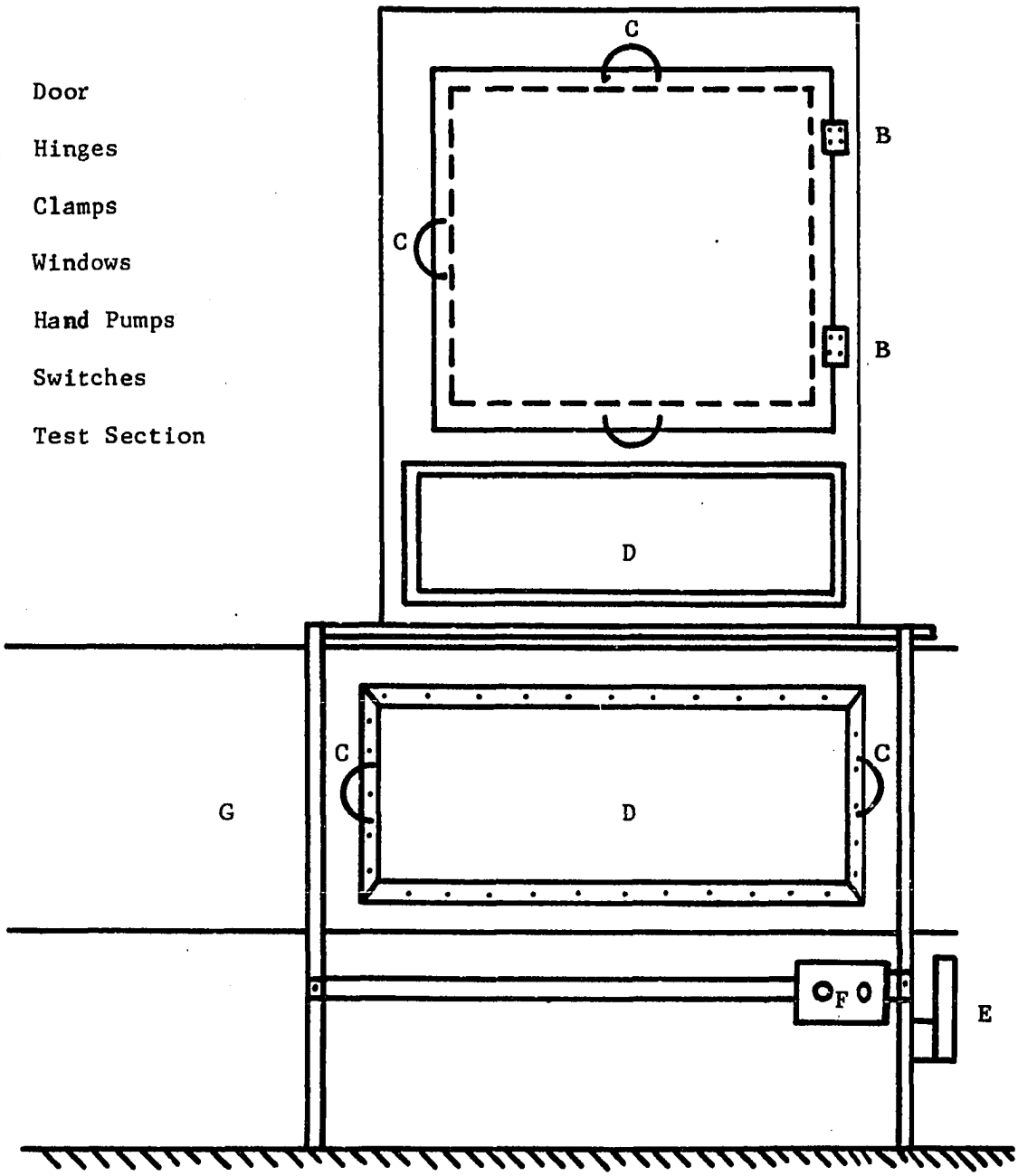

Figure 2-2. Schematic of Balance Box and Test Section for Tunnel 1.

inches was suspended from a steel frame at the upper part of the plywood box with four flexible one-sixteenth inch diameter two feet long steel cables. Four horizontal steel cables were fixed to the steel plate as shown in Figure 2-3. The two in the aft section were connected to two springs. The two in the front were fixed to an aluminum column on which two semiconductor strain gages were installed. A two way motor with variable-speed-control (one to ten rpm) was bolted on the steel plate and was used to change the pitch of the airfoil. The drive shaft of the motor went through a hole in the middle of the steel plate and the rectangular steel channel between the balance system box and the test section ceiling. The shaft was used as the model support.

A long needle was fixed in the center of the steel plate pointing at the marked center of a mirror placed at the lower part of the aluminum measuring column. This needle, when correctly aligned, indicated zero lift on the airfoil.

Tunnel II

Dimensions and Specification

Tunnel II was a return flow, closed throat, atmospheric pressure tunnel. The tunnel was constructed of steel, reinforced concrete gunite and brick (Figure 2-4). The power for the operation of the tunnel was supplied by an Allison V 1710, 1200 horsepower engine. The engine powered a three-bladed seven foot propeller through an extension shaft. The engine, the exhaust manifolds, and the engine oil were water cooled (19).

A. Pitch Control Motor

B. Floating Plate

C. Measuring Column

D. Strain Gages

E. Suspension Wires

F. Model Airfoil

G. Air Hose

H. Springs

I. Test Section

J. Rubber Diaphram

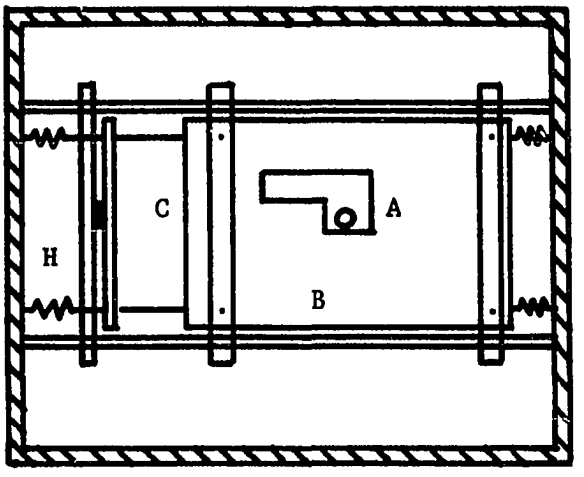

Top View

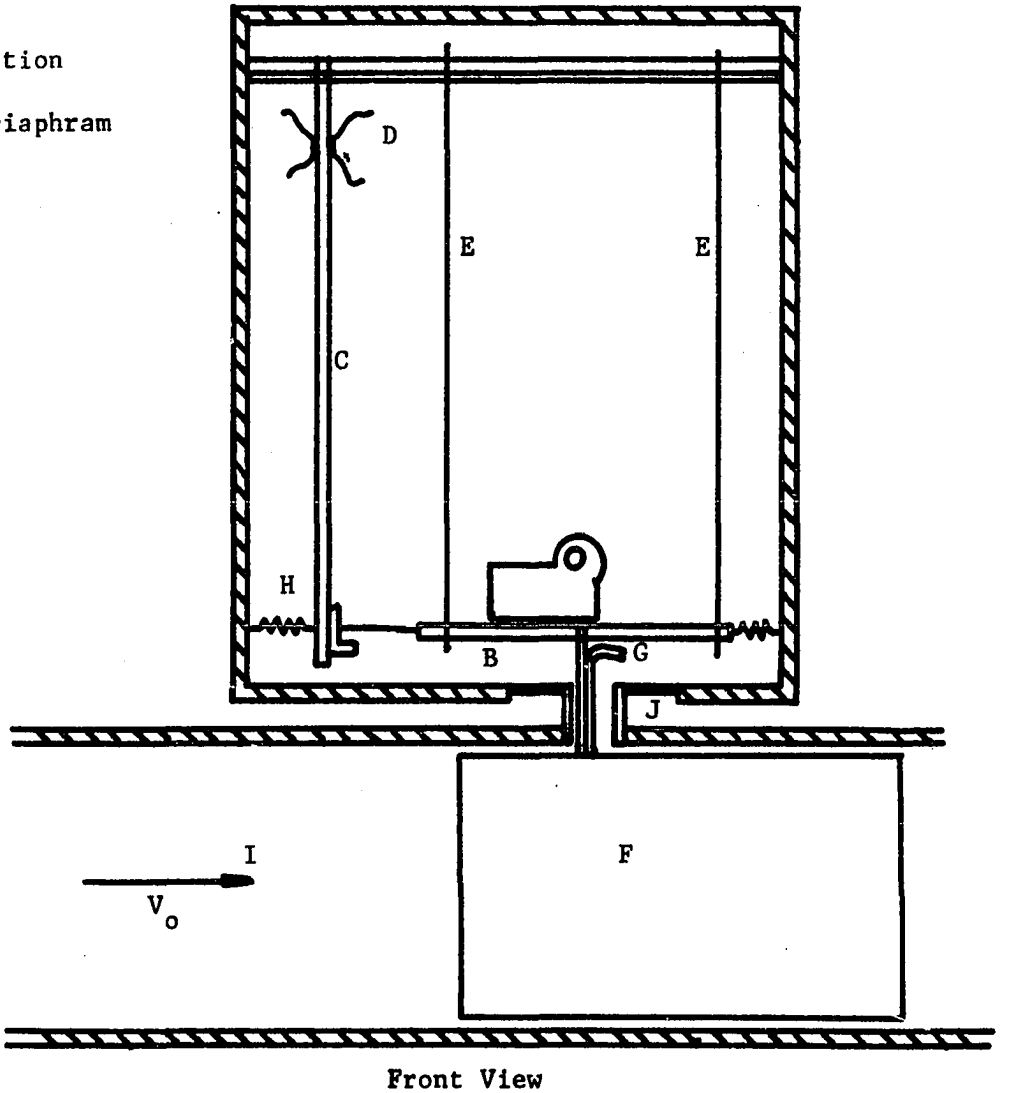

Front View

Figure 2-3. Schematic of Balance System

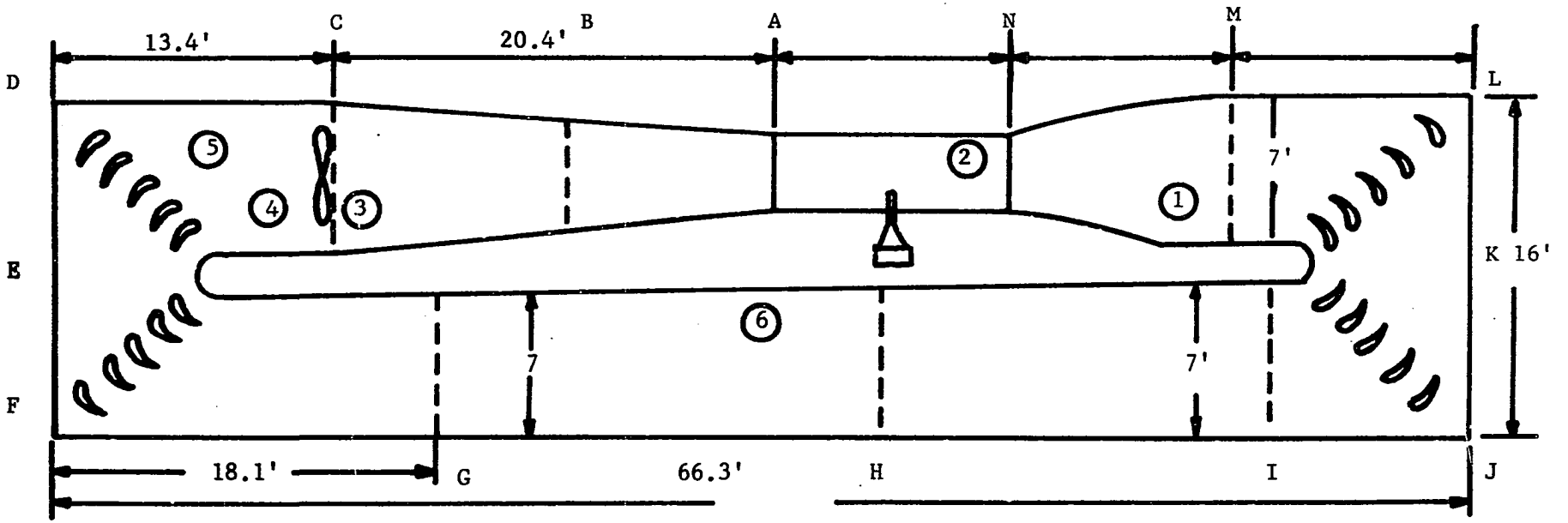

Sta.	Area Sq. Feet
A	20.58
B	31.64
C; ③	38.50
D	47.80
E	58.9
F	57.30
G To M	70.00
N	20.58
④	35.2
⑤	43.3
▷1 ⑥	70.00

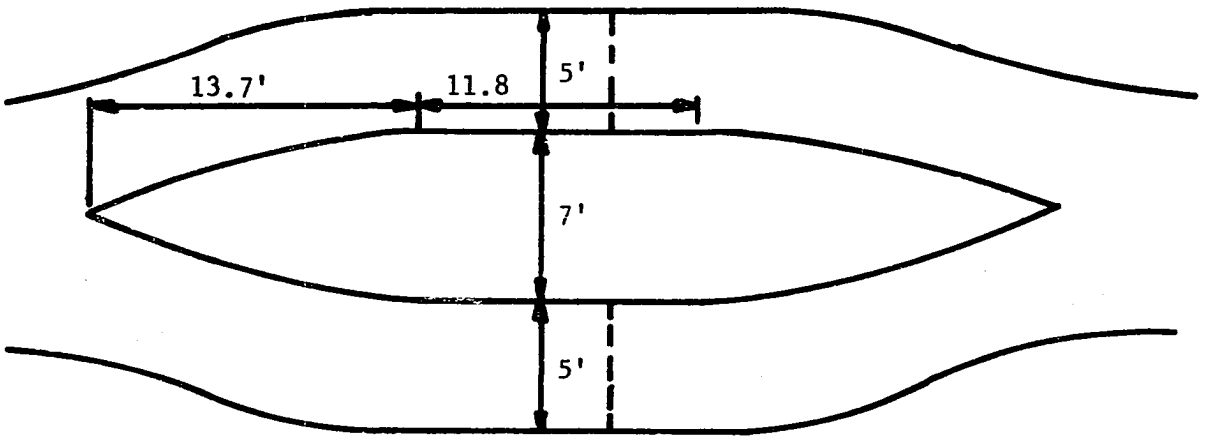

Note ▷1 : Two @ 35 ft^2 Each

Figure 2-4. Schematic of Tunnel 2

The test section was four feet by six feet (approximate ellipse) and eleven feet long. Large access doors of plexiglass and steel frame were located on each side of the test section for convenient model installation. The velocity range was from fifty miles per hour to two hundred miles per hour. At low rpm the engine stalled easily. To achieve low air stream velocity, machine cloth was installed in the diffuser ten feet ahead of the propeller blade. This screen also served as a safety screen between the test section and the propeller, acting as a catch-all in the event of a model failure. The turbulence factor of the tunnel was determined, by using a pressure sphere (16), to be 1.35. The dynamic pressure in the test section was held constant by a pneumatic engine control device operating from the differential pressure between the settling and the test chambers.

The velocity distribution over the test section static pressure was near atmospheric with a very small pressure gradient along its length.

The Breather

Closed-jet tunnels usually required breathers, (20), because the entire return passage was above atmospheric pressure and some air might leak out. In turn, the loss of air would drop the jet pressure below atmospheric unless it were replenished. A slot, at the downstream end of the test section, about .25 inch diameter wide was adapted as the breather for this tunnel.

Corner Vanes

The ideal design for return passage corners would be gradual turns

so the air could follow the curve with but small loss. Such corners would require high construction cost and also a large amount of space. For this tunnel, ninty degree turns were constructed and their losses were kept to a minimum by means of turning vanes.

The Balance System

The balance system was a six component, pyramidal type, utilizing electric resistance strain gauges on aluminum alloy weighing beams. Load intensities were obtained on strain indicators of the SR 4 type. The model was supported on a simple central support. The system was provided with model pitch and yaw adjustments (19).

The advantage of the pyramidal type balance was that the forces and moments on the test model were separated in the balance itself.

The system load capacities were as follows:

LIFT	$\pm \begin{matrix} + 500 \\ - 300 \end{matrix}$ lb.	PITCHING MOMENT	$\pm$1200 in-lb.
DRAG	$\pm$ 200 lb.	ROLLING MOMENT	$\pm$ 500 in-lb.
SIDE FORCE	$\pm$ 150 lb.	YAWING MOMENT	$\pm$ 600 in-lb.

CHAPTER III

MODEL AIRFOILS

The main objective of this research project was to investigate the reduction of skin-friction for a compliant coating surfaced airfoil. In order to eliminate many complicated and laborious mathematical calculations trying to isolate skin-friction drag from pressure and induced drag, the author felt it was necessary to choose a wing section which had very small pressure drag compared to skin-friction drag and test at zero incidence angle in order to eliminate induced drag. As was stated in Chapter I, turbulent boundary layer has a much higher skin-friction drag than laminar boundary layer. The transition line on an airfoil is somewhere around the minimum pressure line. An airfoil with minimum pressure line at the front portion of the airfoil will have a large area under the turbulent boundary layer, resulting in much higher skin-friction drag than an airfoil with large portions of the surface exposed to the laminar boundary layer. A symmetrical airfoil at zero incidence angle theoretically speaking has no spanwise cross flow and could be considered as two-dimensional foil. Comparing wing section data from A.E. Von Doenhoff's "Theory of Wing Sections", NACA 0009 wing meets all the above mentioned factors. Using wing section data (21), and the Von Karman--

Polhausens' method (1), a transition line was calculated. The calculated value was 7.5 percent chord length from the leading edge. This value was very close to the maximum velocity ratio point listed in Table 3-1.

Basically, the compliant coating wings were made of solid material covered with polyurethane foam and polyvinyl chloride (PVC) membrane. From Figure 3-1, it was noticed at about 7.5 percent chord the static pressure was the lowest. This low pressure would cause the PVC membrane to separate from the airfoil and create a tremendous amount of wake drag. This problem was solved by using a vacuum pump with an adjustable valve controlling the amount of suction in order to balance the pressure difference inside the wing section and the test section (Figure 3-4).

Initially the author decided to build a relatively small wing to be tested in Tunnel I, and then test a larger wing in Tunnel II in order to obtain a wider Reynolds number variation.

Wing Construction

Four NACA 0009 wings were constructed, two with a sixteen inch chord, twelve inch span and two, with a forty inch chord, thirty six inch span wings. Each set had one foil with a compliant coating surface and one hard surface airfoil.

The basic construction of the airfoils were the same. The smaller foils had aluminum ribs while the larger foils had redwood ribs. These ribs were bolted together by threaded rods as shown in Figure 3-2. The locations of the rods can be seen in Figure 3-4. The small hard foil was filled with styrofoam, then covered with self

Table 3-1. Basic Information for NACA 0009 Foil

x (per cent c)	y (per cent c)	$(v/V)^2$	v/V	$\Delta v_a/V$
0	0	0	0	0.595
0.5	....	0.750	0.866	1.700
1.25	1.420	1.083	1.041	1.283
2.5	1.961	1.229	1.109	0.963
5.0	2.666	1.299	1.140	0.692
7.5	3.150	1.310	1.145	0.560
10	3.512	1.309	1.144	0.479
15	4.009	1.304	1.142	0.380
20	4.303	1.293	1.137	0.318
25	4.456	1.275	1.129	0.273
30	4.501	1.252	1.119	0.239
40	4.352	1.209	1.100	0.188
50	3.971	1.170	1.082	0.151
60	3.423	1.126	1.061	0.120
70	2.748	1.087	1.043	0.095
80	1.967	1.037	1.018	0.070
90	1.086	0.984	0.992	0.046
95	0.605	0.933	0.966	0.030
100	0.095	0	0	0
L.E. radius: 0.89 per cent c				

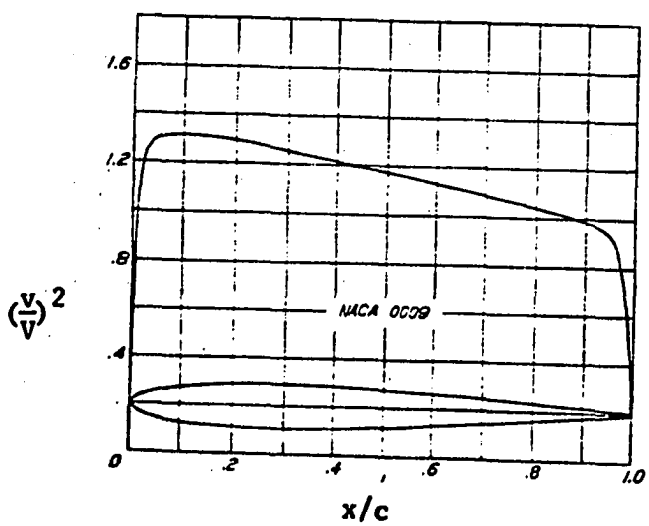

Figure 3-1. Cross section of NACA 0009 Airfoil

adhesive vinyl paper which gave a very smooth protective surface. The small soft airfoil was filled with styrofoam and channels were built inside the styrofoam. The styrofoam was covered with one layer of 3/16 inch thick forty pores-per-inch (PPI) polyurethane foam and various thicknesses of PVC skin (ranging from 0.001 to 0.0035 inches). (Figure 3-3) The leading edge of the larger foils was made of solid balsa wood covered with a layer of 1/16 inch thick balsa to achieve uniform curvature and smooth surface along the leading edge. The remainder of the larger foils was covered with twenty-two gauge sheet metal (Figure 3-4). The screw dimples caused by screws used to fasten sheet metal to the redwood ribs were filled with hard wax. The soft foil was covered with one layer of 1/8 inch thick 20 PPI polyurethane foam and one layer of 1/8 inch thick 40 PPI polyurethane foam, and then the PVC skin. One-sixteenth inch diameter holes were drilled on the metal skin to allow vacuum suction on the larger foils. On the smaller foil the porous styrofoam precluded any need to drill holes to the surface.

The PVC was attached to the airfoil ends by using, double stick scotch tape. To achieve a smooth surface, self adhesive vinyl paper was used on both edges of the foil to cover the PVC and the scotch tape.

Before the airfoil was installed three hundred pounds of steel was put on the foil to test the strength of the structure. (Figure 3-5).

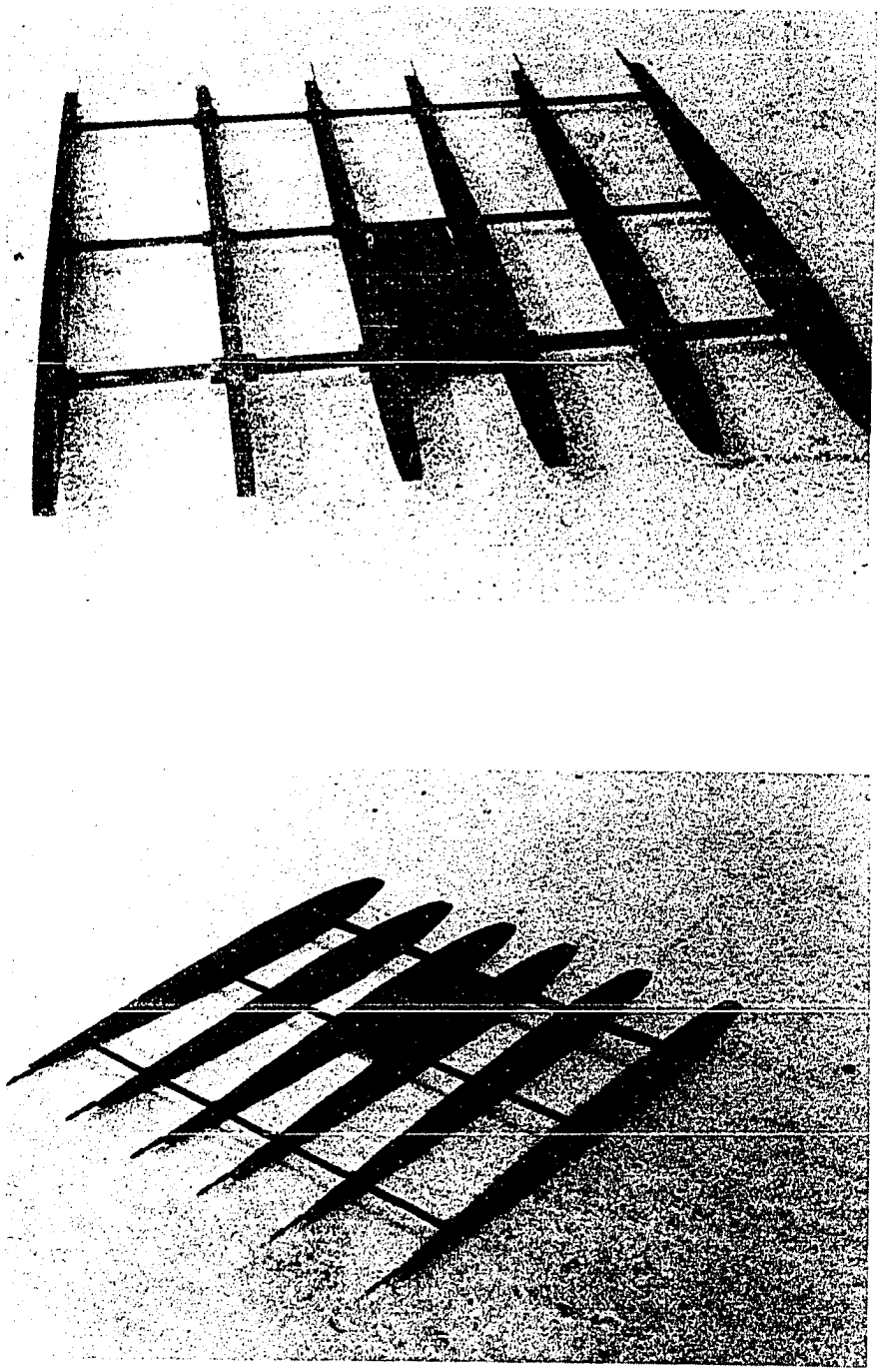

Figure 3-2. Basic Structure of the Model Airfoil

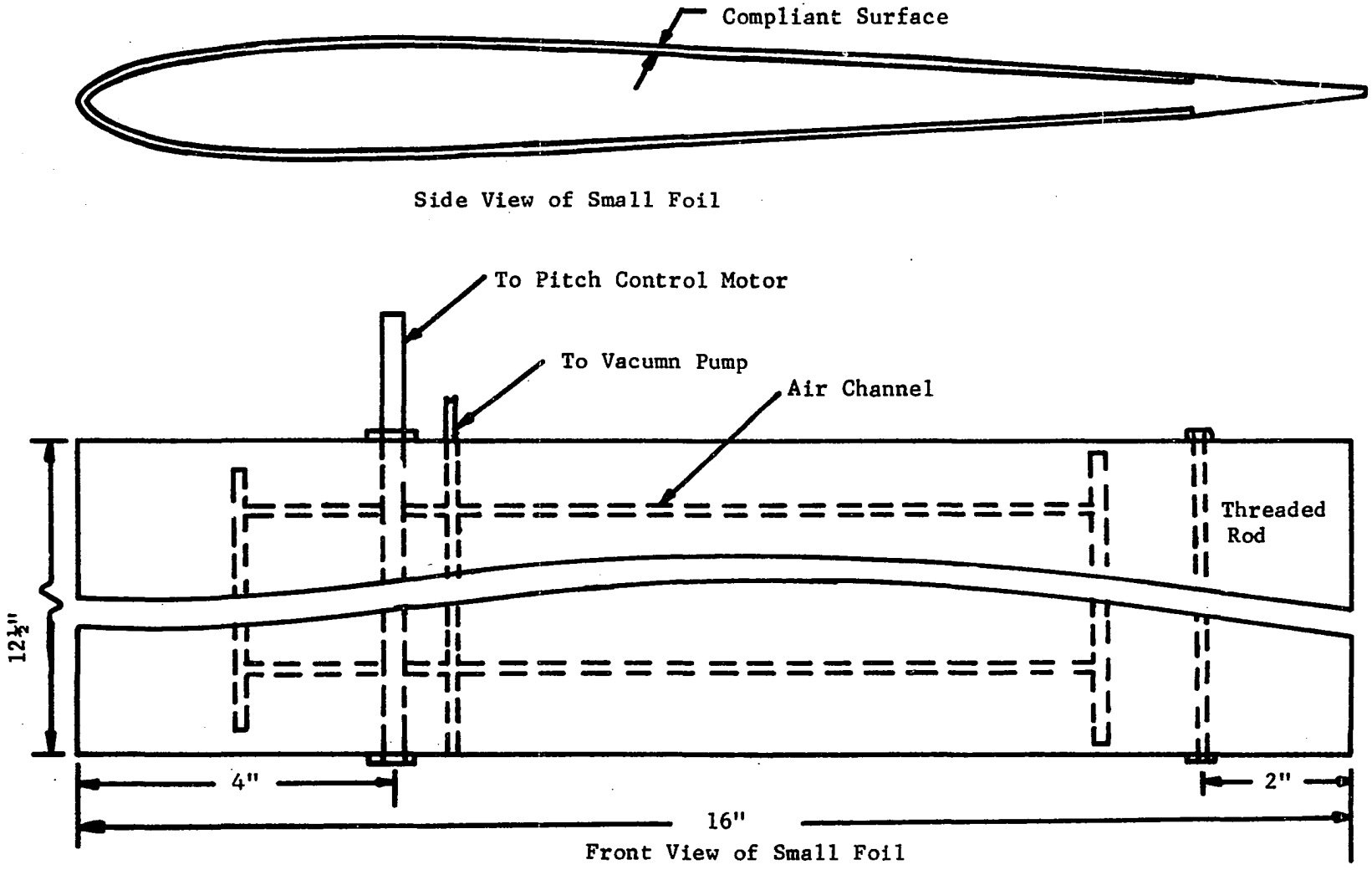

Figure 3-3. 16" NACA 0009 Airfoil

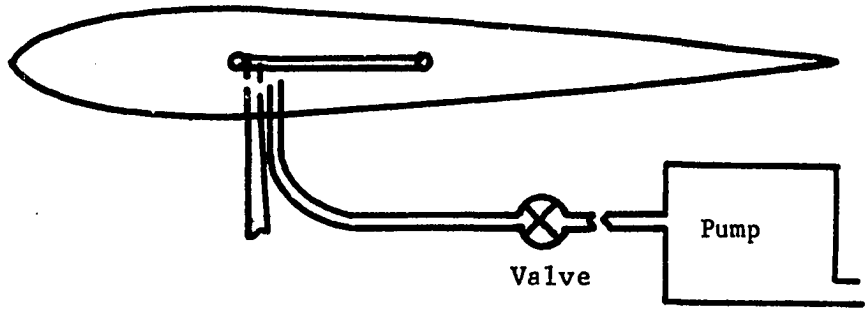

Side View

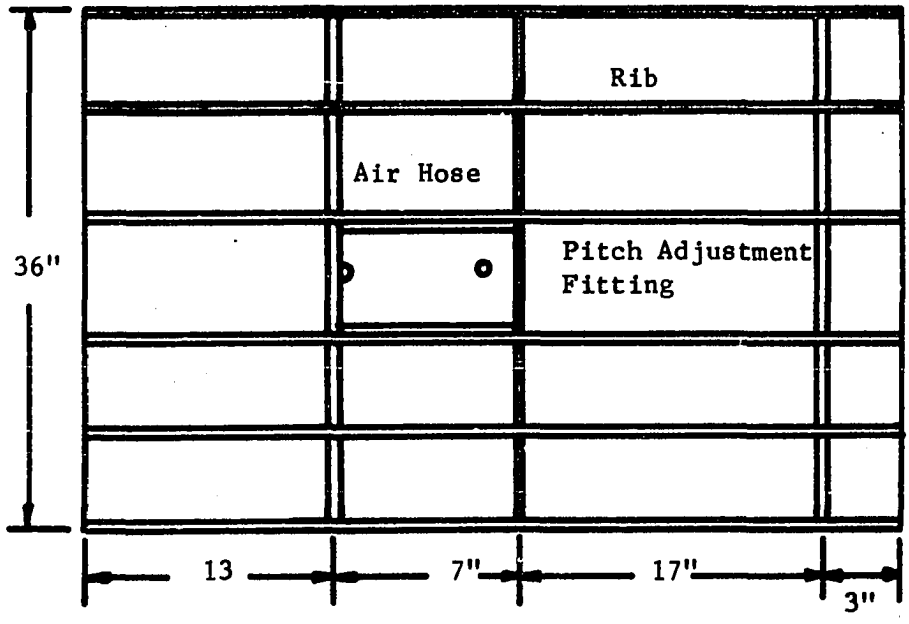

Front View

Figure 3-4. 40" Chord 0009 Air-Foil

Figure 3-5. Static Structure Test

CHAPTER IV

THE POSITION OF TRANSITION ON AN AIRFOIL

BY

VON KARMAN & POHLHAUSENS' APPROXIMATION METHOD

To determine the transition point on an airfoil by complete calculation of the boundary layer for a given body with the aid of the boundary layer differential equations is very time consuming and difficult. A less difficult and quicker method is the Von Karman-Pohlhausen integral method (1).

Pohlhausen uses Von Karman's momentum integral equation,

$$\frac{\tau_o}{\rho} = U^2 \frac{d\theta}{ds} + (2\theta + \sigma^*)\, U \frac{dU}{ds} \qquad (1)$$

to find his solution. S is the arc length measured from the stagnation point along the wetted surface. This equation gives an ordinary differential equation for the boundary layer thickness. With the introduction of two shape factors

$$\Lambda = \frac{\sigma^2}{\nu} \frac{dU}{ds}$$

and

$$K = \frac{\theta^2}{\nu} \frac{dU}{ds}$$

together with new variables,

$$z = \frac{\theta^2}{\nu} \quad ; \quad f_1(K) = \frac{\sigma^*}{\theta} \quad ; \quad F(K) = U \frac{dz}{ds}$$

equation (1) can be reduced to

$$\frac{dz}{ds} = \frac{F(K)}{U} \tag{2}$$

where F(K) is a complex function of Λ only. Therefore, as far as the solution of Equation (2) is concerned, F(K) can be calculated once and for all for various values of Λ , F(K) are listed in Table 12.2 of Schlichting (1).

A. Walz (17), showed that equation (2) can be further reduced to a simple quadrature by approximating F(K) with a straight line,

$$F(K) = a - bK$$

Equation (2) can be reduced to,

$$U \frac{dz}{ds} = a - bK \tag{3}$$

letting $K = \frac{\theta^2}{\nu} \frac{dU}{ds}$ and then substituting z and K into Equation 3,

$$U \frac{d\theta^2}{ds} = a - b \frac{\theta^2}{\nu} \frac{dU}{ds}$$

which reduces to

$$\frac{d}{ds} \left(U \frac{\theta^2}{\nu}\right) = a - (b-1) \frac{\theta^2}{\nu} \frac{dU}{ds} \tag{4}$$

Using the Thwaite approximation, with a = 0.45; b = 6.

$$\frac{d}{ds}\left(U\frac{\theta^2}{\nu}\right) = 0.45 - 5\,\frac{\theta^2}{\nu}\,\frac{dU}{ds}$$

Upon separating the variables and integrating, one obtains

$$\frac{U\theta^2}{\nu} = \frac{0.45}{U^5}\int_{s=0}^{s} U^5\,ds$$

The non-dimensional variables are then substituted so that

$$z^* = \frac{\theta^2\,U_o}{\nu\,\ell} \quad ; \quad s^* = \frac{s}{\ell} \quad ; \quad U_m = \frac{U}{U_o}$$

$$z^* = \frac{\theta^2\,U_o}{\nu\,\ell} = \frac{0.45}{U_m^{\,6}}\int_o^{s^*} U_m^{\,5}\,ds^*$$

and z^* can then be evaluated by graphical integration.

Since,

$$\frac{\sigma^*}{\theta} = f_1(K)$$

$$K = \frac{\theta^2}{\nu}\,U^*\,\frac{U_o}{\ell}$$

$$\theta = \left(\frac{K\nu\ell}{U_o U^*}\right)^{\frac{1}{2}}$$

therefore,

$$\sigma^*\left(\frac{U_\infty\,U'_m}{K\,\nu\,\ell}\right) = f_1(K)$$

But

$$\frac{U'^{*}_{m}}{K} = \frac{1}{z} \quad \text{from above equation}$$

so,

$$\frac{\sigma^{*}}{\ell}\sqrt{\frac{U_o \ell}{\nu}} = f_1(K)\sqrt{\frac{V_o \ell}{\nu}}$$

and $f_1(K)$ is listed in Table 12.2 of Schlichting (1). σ can be determined at this point. $\sigma^{*} U_m/\nu$ can also be determined, and this value for each point along the body will be compared with Figure 17-3 in Schlichting (1). Transition points can then be easily determined. Transition occurs when $(U \sigma^{*}/\nu) > (U \sigma^{*}/\nu)_{crit.}$.

Results of calculation for NACA 0009 airfoil for the most frequent tested speed range for this experiment are listed in Table 4.1.

Von Doenhoff (21), predict that transition should start around the minimum pressure point. Figure 3.1 shows the minimum pressure for NACA 0009 is at 7.5% chord. The calculations in Table 4-1 show that the theoretical transition is close to the 7.5% chord position.

Table 4-1. Parameters for Transition Calculation

x/ℓ	s/ℓ	v/U_o	z^*	$\frac{\sigma^*}{\ell}\sqrt{\frac{U.\ell}{\nu}}$	$\frac{(U\sigma^*)/\nu}{U_o=120 \text{ ft/sec}}$	$U_o=100 \text{ ft/sec}$	$U_o=80 \text{ ft/sec}$	$(\frac{U\sigma^*}{\nu})^{**}_{crit.}$
0	0	0	.00096	.071	0	0	0	10000
.005	.01	.866	.0024	.1178	137	125.4	111	3500
.0125	.02	1.041	.00343	.1433	200	183.3	162	2500
.025	.0349	1.109	.00778	.2702	330	300.3	266	1200
.050	.0607	1.140	.0184	.3315	510	464.8	404	980
.075	.0868	1.145	.0280	.4199	646	591.3	516	680
.100	.1129	1.144	.0385	.5025	774	707.07	617	570
.15	.1636	1.142	.0585	.62	850	821.65	760	550

** From Figrue 17.3 Schlichting

CHAPTER V

Flow Visualization

There is no simple theoretical method that the author can use to predict a transition point on the compliant coating airfoil. It was felt necessary to develop a flow visualization method to locate the transition point for both the solid and compliant coating wing sections.

Three techniques which have been used in the past are tufts, oil films, and diffusible chemical solids. For preliminary tests, the tuft model was set up, but it was very hard to determine the exact point of transition. The oil films method was also tried, but without success because PVC reacted with the hydrocarbon. PVC skin coated with oil wrinkled and became loose. The only alternative left was chemical solid. It is a physical property of china clay that if a solution has the right index of refraction is spread on the top of a film of china clay, it will become transparent. After the solution evaporates the china clay will turn to its original white color. This property along with the principle that the rate of evaporation of certain organic chemicals is much lower in a laminar flow than in a turbulent flow will show the exact transition line. Most solutions used by other investigators will react with PVC. Water

will not react with PVC, but has a wetting problem; it forms drops instead of a thin film unless heat is applied. However, heat has unfavorable effects on PVC. After many weeks of trial and error attempts, finally a successful combination of solvent and solution was found. PVC soaked in acetone for an extensive period of time will react. However, if the acetone is sprayed on PVC, they will not react because the contact time is too short, due to the evaporation of the acetone. With the help of an ultra-sonic vibration bath, located in the School of Geology, at the University of Oklahoma, china clay was suspended in acetone. The particles in the suspensions are so fine they can be spread on an airfoil and form a thin film without affecting the flow pattern on the airfoil.

For better visualization, the airfoils were painted black, then acetone-suspended china clay was sprayed on the airfoil. The airfoil turned white. Ethylene glycol was sprayed on the airfoil. This step made the white film transparent and became black again. The tunnel engine was started and after a few minutes, part of the foil in the turbulent region turned white and the portion in the laminar region remained black. Figure 5-1 and Figure 5-2 were both taken at ninty feet per second air speed and four minutes after the tunnel was turned on. The transition on both compliant coating airfoil and hard surface airfoil occured at around 9 percent chord. This value agreed with the previous calculation.

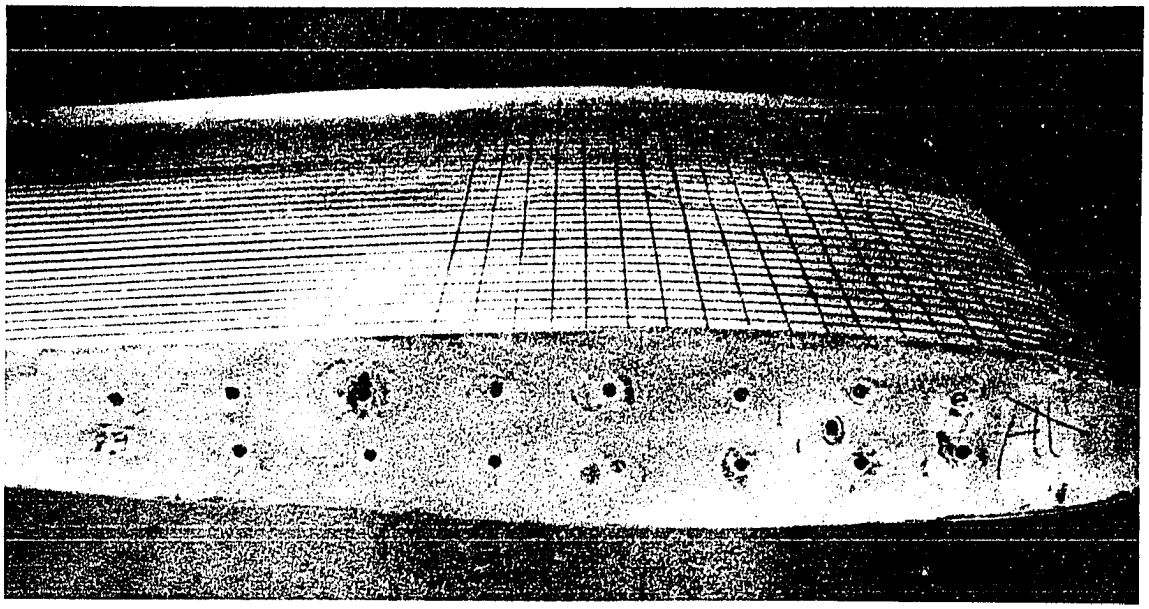

Figure 5-1. Transition Line on Compliant Coating Airfoil

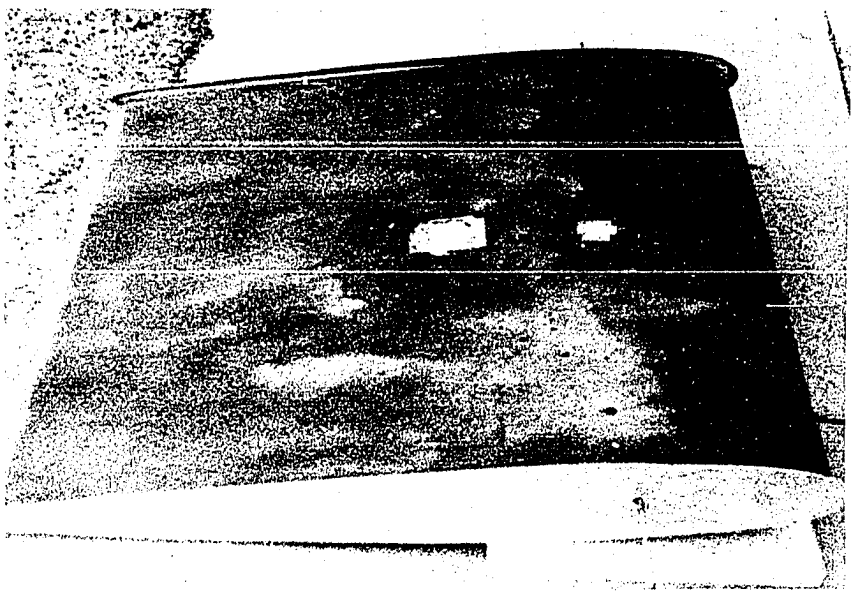

Figure 5-2. Transition Line on Hard Surface Airfoil.

CHAPTER VI

CALIBRATION AND EXPERIMENTAL PROCEDURES

Calibration of Tunnel Speed

In an ideal wind tunnel using an ideal fluid, the calculated velocity using Bernoulli's equation would be equal to the actual velocity in the tunnel. Since no wind tunnel is ideal, a correction factor K_c must be introduced into the calculations to produce the actual velocity of the fluid.

To determine K_c the pressure differential was obtained at the bellmouth and the test section (see Figure 2-1 and Figure 2-2). This was done by means of a manometer connected to each section. Let Section 1 be the bellmouth section and Section 2 the test section. Let K_1 be the loss coefficient between the sections and assume ρ constant.

From Conservation of Energy

$$P_1 + q_1 = P_2 + q_2 + K_1 q_2 \qquad (6.1)$$

From continuity,

$$A_2 V_2 = A_1 V_1 \qquad (6.2)$$

Squaring both sides and multiplying by $\rho/2$, gave

$$\frac{\rho}{2} A_2^2 V_2^2 = \frac{\rho}{2} A_1^2 V_1^2$$

But

$$q = \frac{\rho V^2}{2}$$

So,

$$q_2 A_2^2 = q_1 A_1^2$$

Solving for q_1,

$$q_1 = q_2 \left(\frac{A_2}{A_1} \right)^2$$

$$q_1 = q_2 K_2$$

where $K_2 = \left(\frac{A_2}{A_1}\right)^2$

From Equation 6.1, the change in P between section 1 and 2 could be calculated as follows:

$$P_1 - P_2 = q_2 + K_1 q_2 - K_2 q_2$$

$$P_1 - P_2 = q_2 (1 + K_1 - K_2)$$

$$\Delta P = K_3 q_2 \quad \text{where } K_3 = (1 + K_1 - K_2)$$

$$\Delta P = P_1 - P_2$$

$$\Delta P = \frac{\rho V_2^2}{2} \quad (K_3)$$

$$V_2^2 = \frac{2}{K_3} \quad \left(\frac{\Delta P}{\rho}\right)$$

$$V_2 = K_4 \sqrt{\Delta P/\rho}$$

For a given wind tunnel test, barometric reading, temperature at barometer and relative humidity in tunnel after runs were obtained. The pitot tube was set on the tunnel center line. Fifteen readings over the operating speed range of the tunnel were taken.

The calculated values for K_4 for tunnel 1 and 2, respectively, were 3.334 and 3.385.

Curves for ΔP and velocity for three values of ρ are shown in Figure 6-1 and Figure 6-2.

Velocity Survey

Before a wind tunnel is used for experiments, the local velocities in the test section must be investigated in order to determine the tunnel flow characteristics. Local velocity variations may be measured across the test section by means of a pitot-static tube using

$$V = \left(\frac{2q}{\rho}\right)^{\frac{1}{2}}$$

The velocity maps for tunnel 1 and tunnel 2 are shown in Figure 6-4 and Figure 6-5.

Calibration of Balance System

The basic measuring mediums for both tunnels are aluminum alloy beam, strain gage and strain gage indicator. The load on the beam changes the gage resistance. It is necessary to correlate the load force and resistance change shown on the indicator.

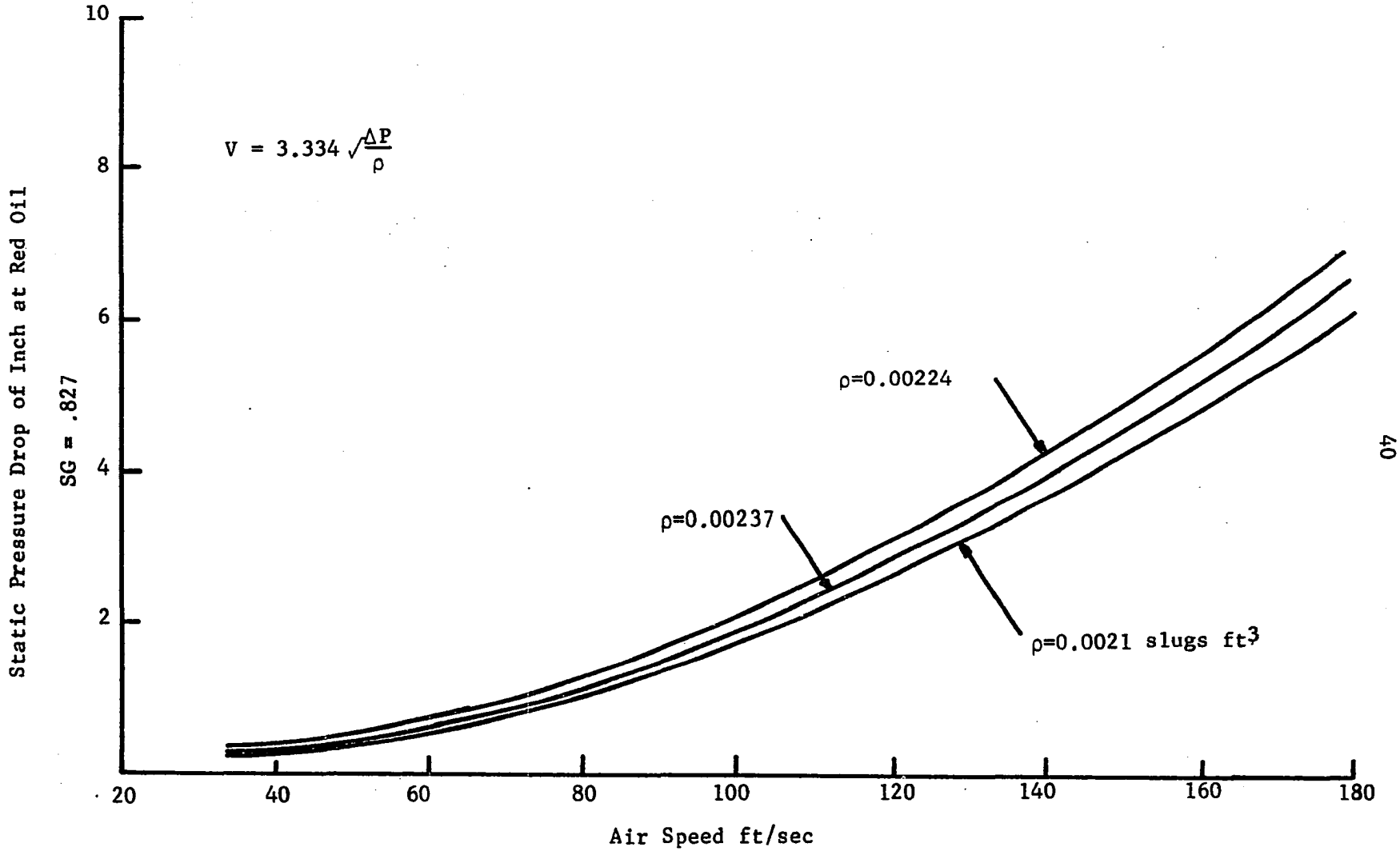

Figure 6-1. Free Stream Velocity Calibration for Tunnel I.

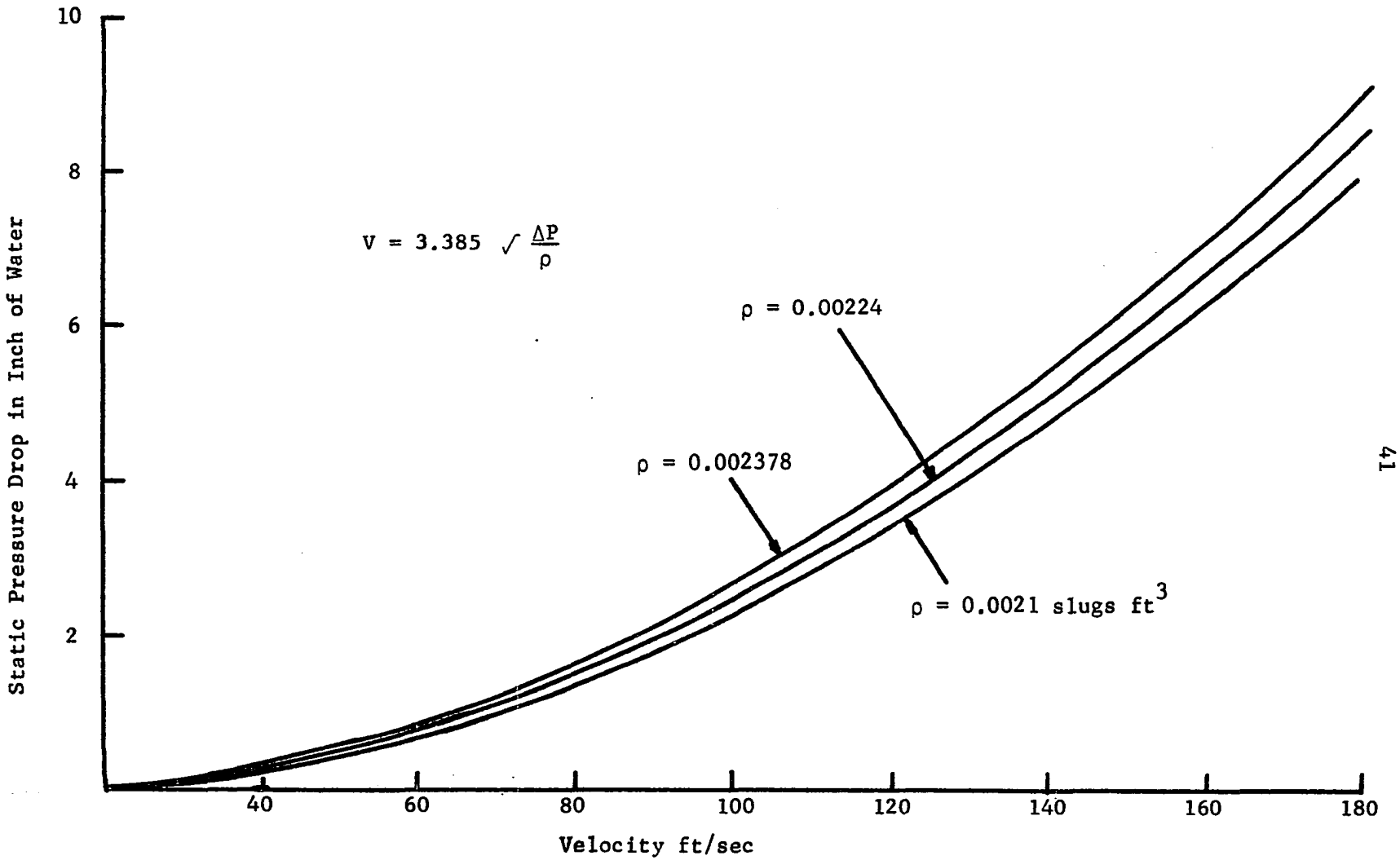

Figure 6-2. Static Pressure Drop Versus Velocity for Tunnel II

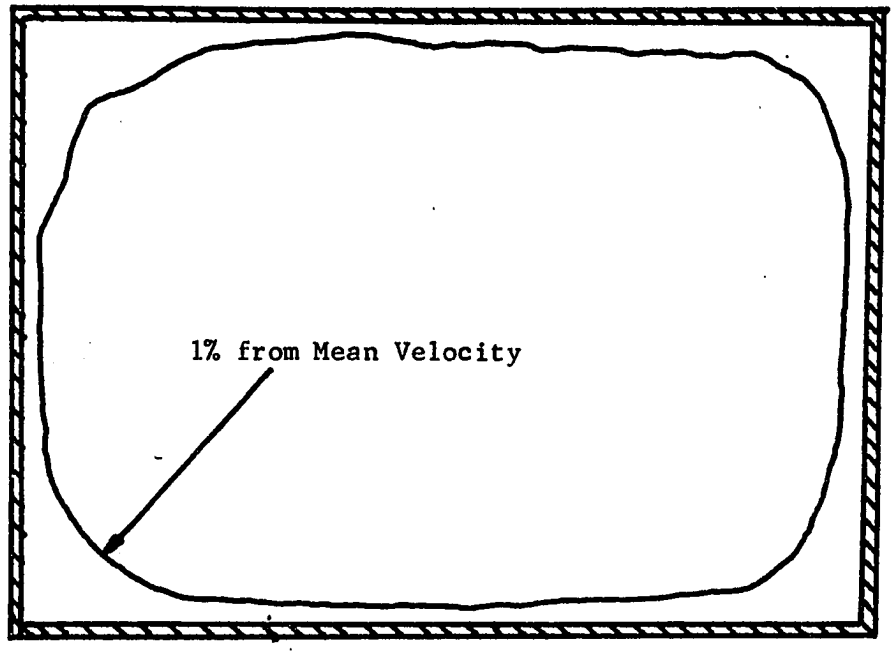

Figure 6-3. Velocity Distribution of Tunnel I.

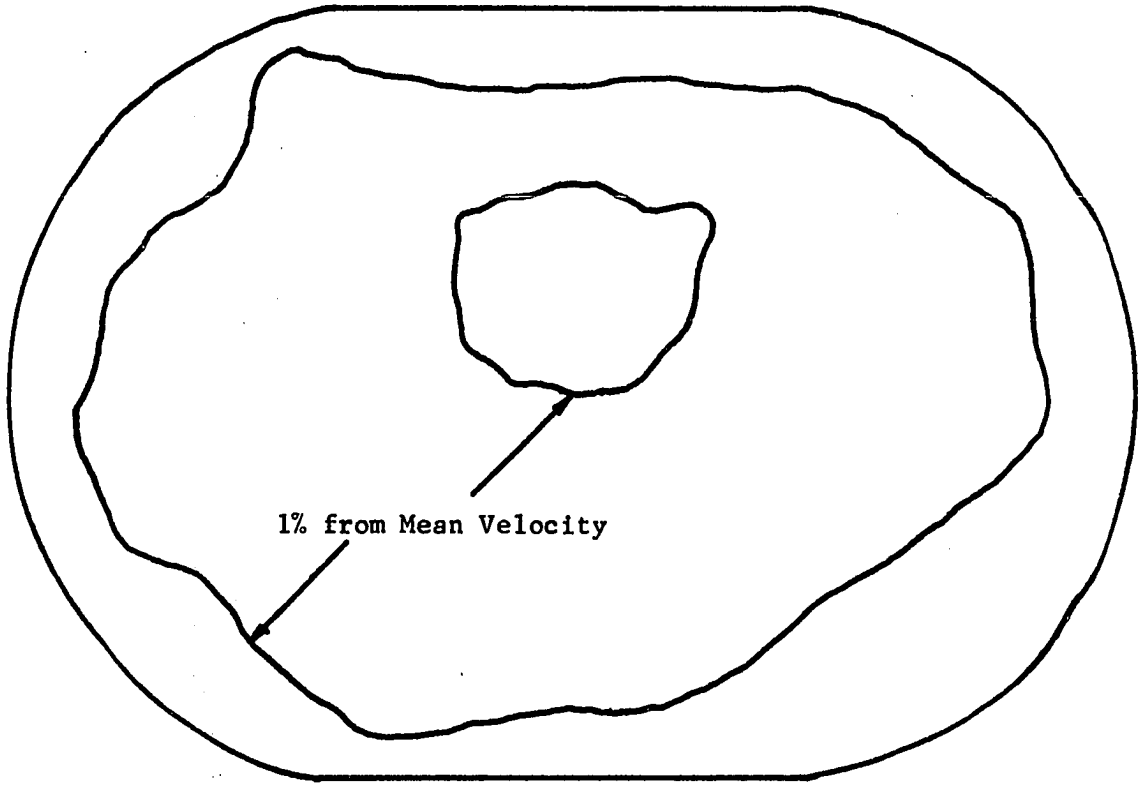

Figure 6-4. Velocity Distribution of Tunnel II. Ref. Comp-(19)

For tunnel I a set up shown in the Figure 6-5 and weights ranging from 0.116 to 1.0 lb. were used. Different weights were placed in A and corresponding readings from the strain gage indicator were recorded. The results are shown in Figure 6-6.

A. Weight Holder

B. Floating Plate

C. Strain Gages

D. Pulley

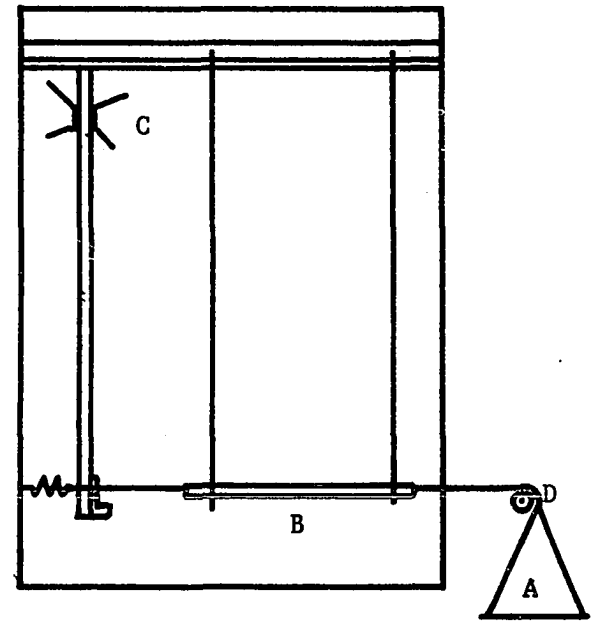

Figure 6-5. Schematic of Strain Gage/Force Calibration System for Tunnel I

For tunnel II, the set up (Figure 6-7) used weights ranging from .5 lb. to 10 lb. Special care was taken to line-up "C" and "B" on the same level. The results are shown in Figure 6-8.

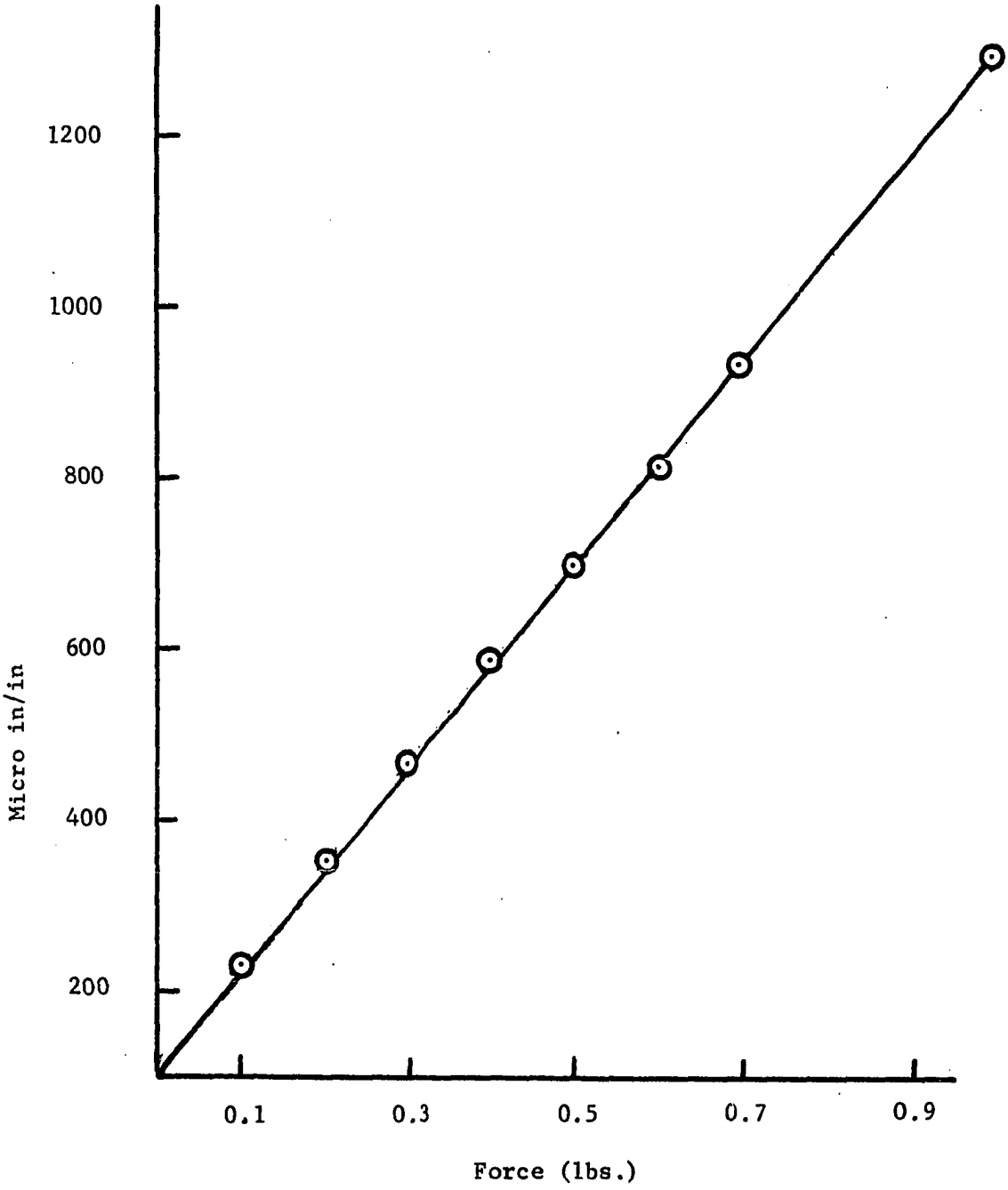

Figure 6-6. Balance System Force/Strain Calibration for Tunnel I

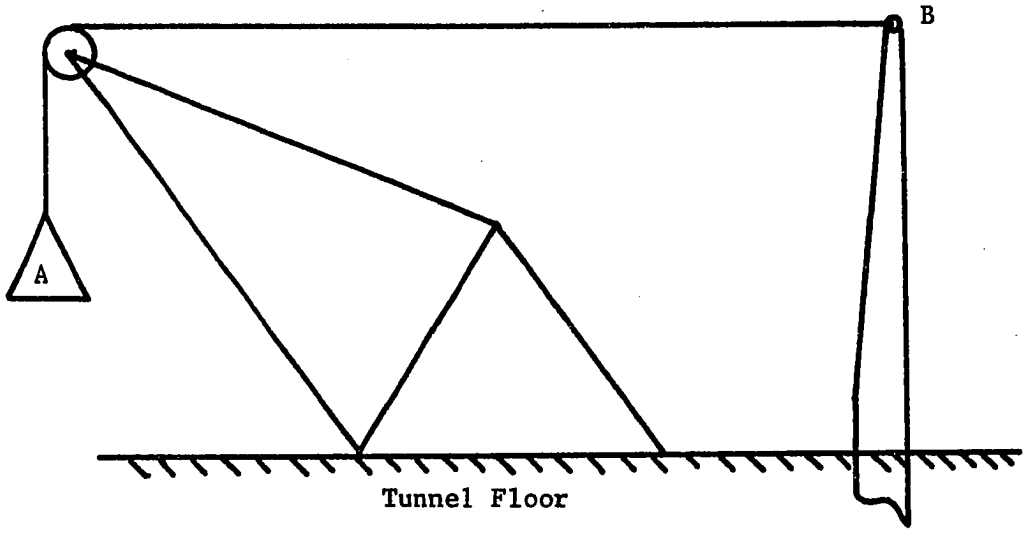

A. Weight Holder B. Balance Resolving Point

Figure 6-7. Schematic of Strain Gage/Force Calibration System for Tunnel 2

Experimental Procedure

With the systems calibrated, the primary task of obtaining data was now ready to proceed. Tuft models were prepared for both tunnels to ensure that there was no apparent cross flow and separation.

Tunnel 1

The hard surface airfoil was mounted vertically in the test section (Figure 6-9). The balance system and airfoil were allowed to settle, then needle "G" was adjusted in such a manner so the image of "G" on mirror H passed through the marked line on "H" when the operator viewed through reference line on window (Figure 6-9). Throughout the test this condition was maintained to ensure that there was no lift force exerted on the airfoil by the flow. The

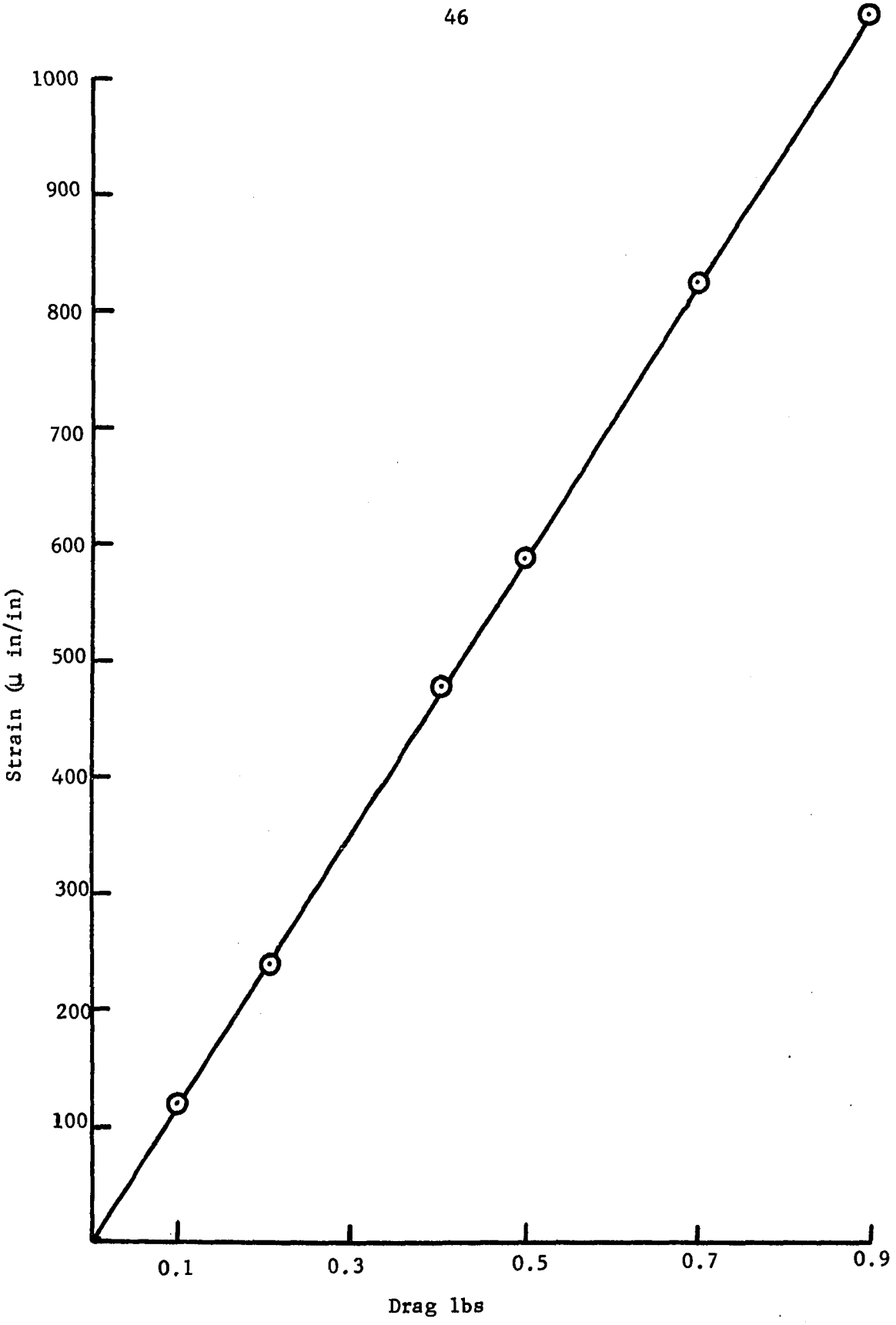

Figure 6-8. Balance System Force vs. Strain Calibration For Tunnel II .

reasoning behind this was that any position change of the needle corresponded to a change in elevation of the steel plate and the foil. This change of elevation indicated lift force on the airfoil. The minimum noticeable change of position of the needle corresponded to .002 lb. force. This proved the system to be sensitive and satisfactory. The two way electric motor"A" was used to align the airfoil with the tunnel center line by eye sight. The speed control vanes were adjusted so that minimum tunnel speed was maintained when the tunnel was turned on, The speed of the tunnel was increased to about 150 ft/sec. "N" was used to line the "H" needle to keep the lift force at its minimum. The tunnel was turned off and the vanes were readjusted to their original position. Barometric pressure, temperature, strain gage indicator readings, and manometer readings were recorded. After the balance system settled the tunnel was turned on again. Tunnel air stream speed was increased in small increments and corresponding manometer readings for ΔP, and strain gage indicator readings were recorded. After reaching the highest air speed ,the air speed was slowed down by small increments. Manometer and strain gage indicator readings were again recorded. The same procedures were repeated at least three times for each set of data.

For the soft skin airfoil the procedures were about the same except, before the tunnel was turned on, the suction vacuum pump was adjusted. Proper vacuum could easily be obtained by comparing the test section static pressure with the vacuum pressure drop.

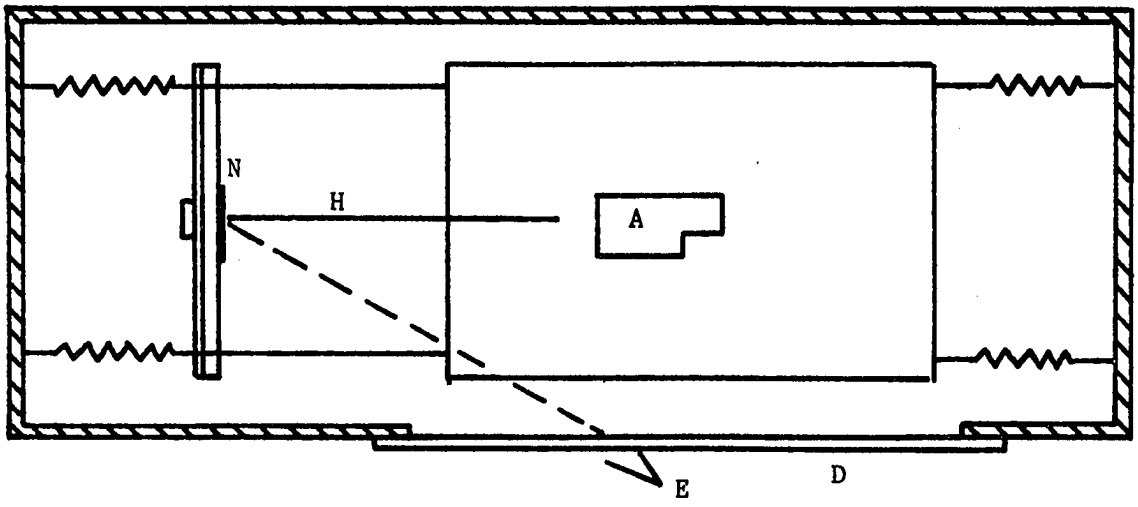

A. Pitch Control Motor

H. Pointer Needle

N. Mirror

D. Window

E. Guide Line

F. Airfoil

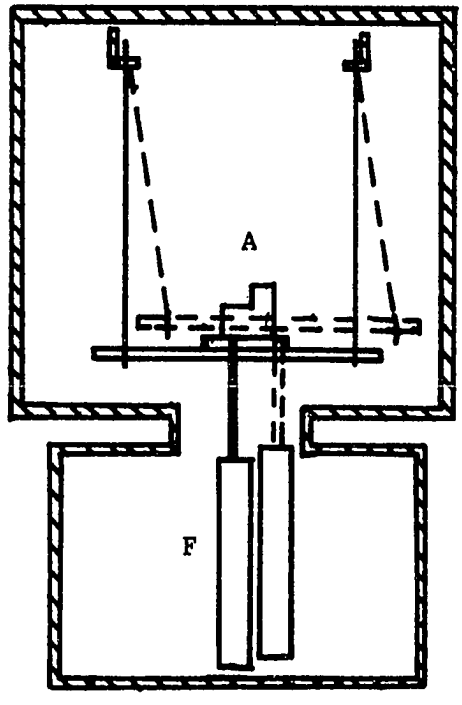

Figure 6-9. Schematic for Zero Lift Indicating System.

Tunnel 2

The airfoil in tunnel 2 was mounted on a bayonet which was shielded by a windshield. (Figure 6-10). A tare drag was contributed by the bayonet and pitch adjustment mechanism. The interference between the windshield, bayonet and pitch adjustment mechanism changed the drag reading also. It would be almost impossible to calculate all these interference effects.

The standard method for a symmetrical airfoil with zero angle of attack is to measure the drag force of the airfoil including the drag force on the bayonet, pitch mechanism and the interference with the model and the windshield. Then, image bayonet, pitch adjustment mechanism and windshield are installed. The difference of the two tests indicates the drag on bayonet, pitch adjustment mechanism, and interference among windshield, bayonet and the model. All models tested in tunnel 2 were tested twice, first with dummy image, then without image.

With all systems calibrated, the wing was mounted in the tunnel. Strain gage locks for all six force and moment components were released. The airfoil was first aligned by adjusting the pitch and yaw control mechanism. The test section windows were closed. The clutches for yaw and pitch adjustment mechanism were released. Barometric pressure,temperature, initial readings of strain gage indicators for yaw, lift, and drag forces were recorded. The engine control system was switched to manual operation. A signal was given to engine room operator to start the engine. The vacuum pump for

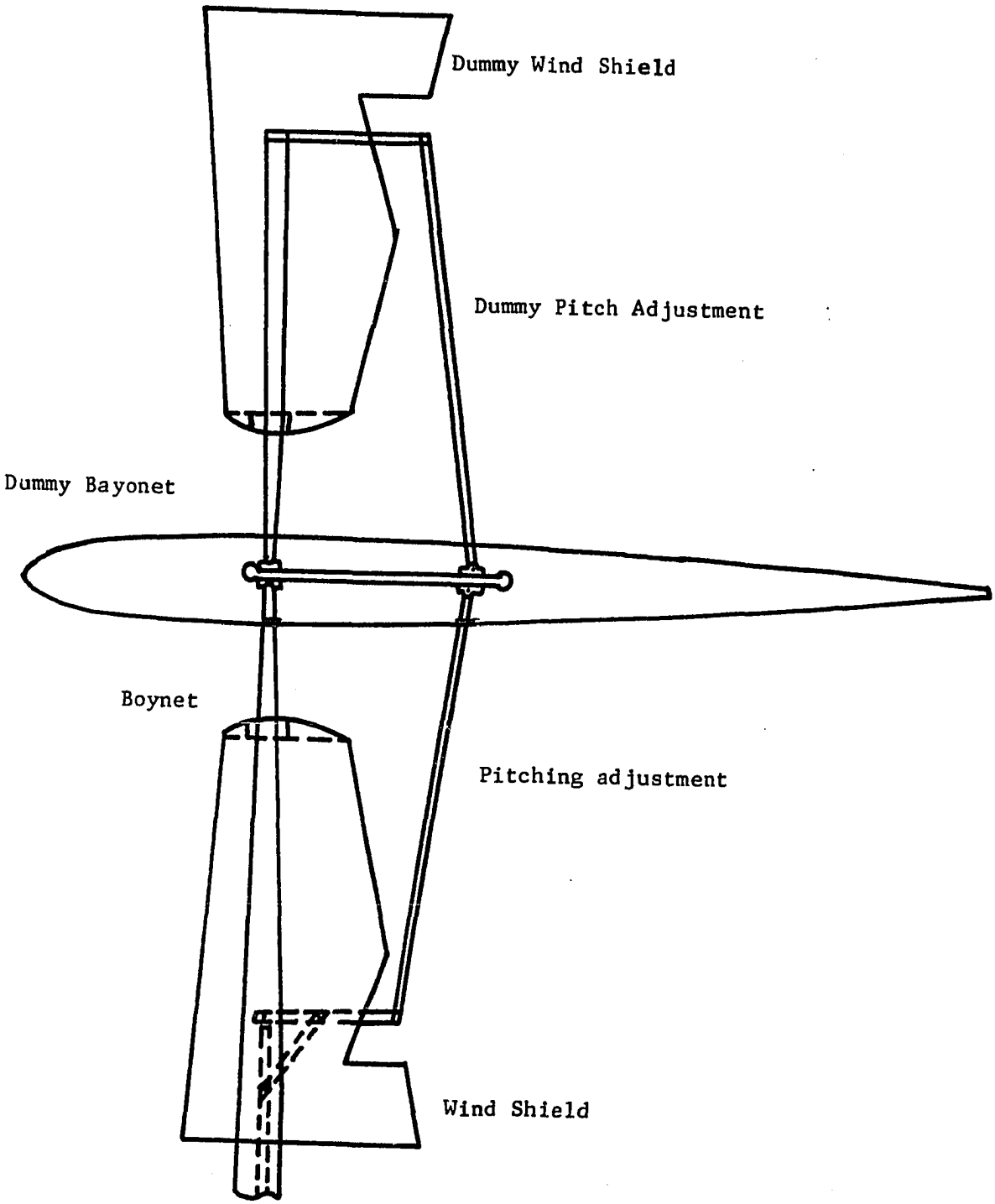

Figure 6-10. Wing Section Setup in Tunnel II. (With Dummy Wind Shield).

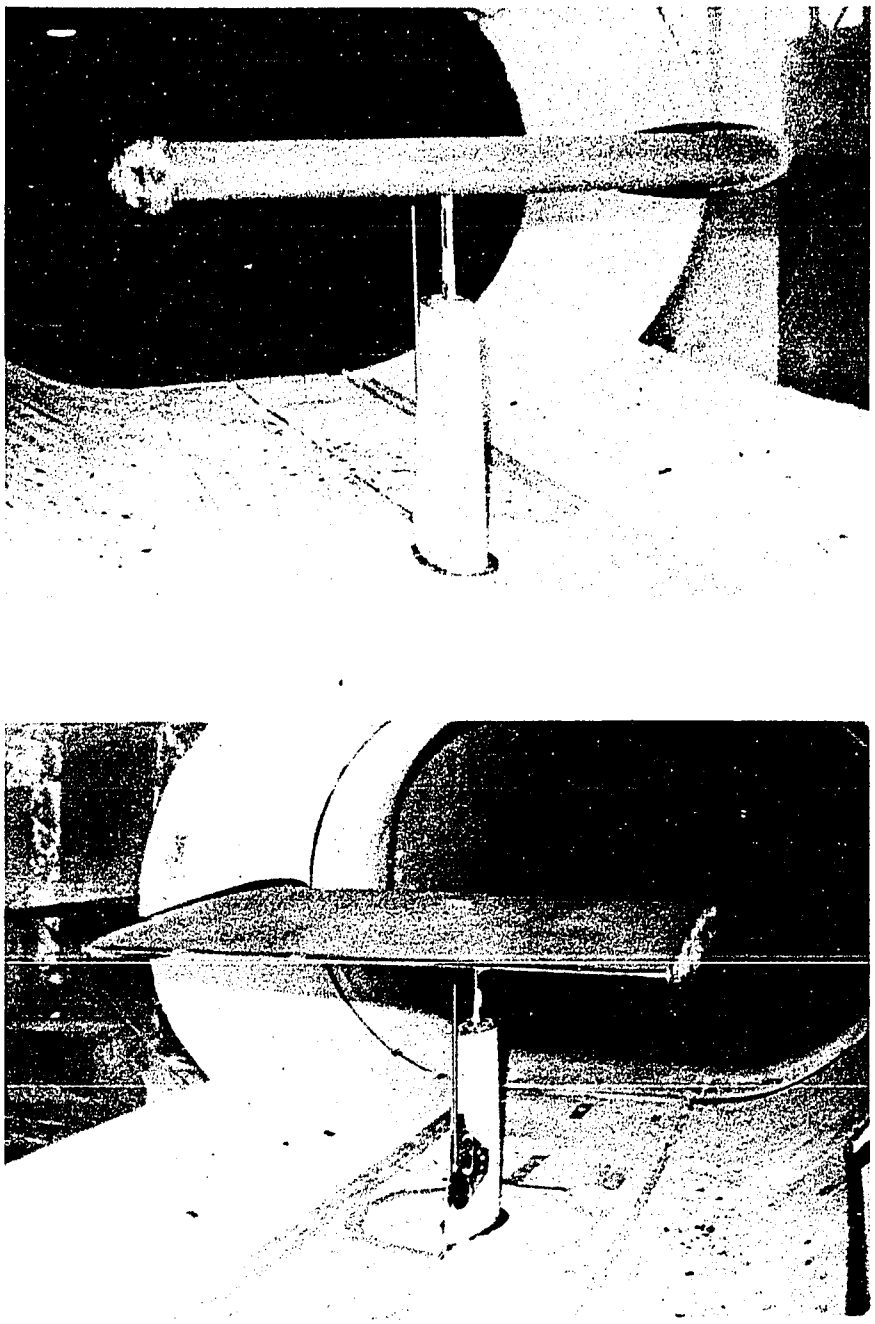

Figure 6-11. 40" 0009 Airfoil in Tunnel II

balancing pressure between test section and inside the foil was then turned on. It took about five minutes to warm up the engine and for the flow to reach steady state. Yaw and pitch mechanism were again engaged and adjusted so that there was no yaw and lift forces on the airfoil. The clutches were released again and data were taken. The air speed was increased in small increments. For each speed tested, tunnel temperature, static pressure difference, and strain gage indicator reading for drag were all recorded. From time to time, yaw and lift forces were monitored to insure that there was no induced drag. The test speed range was from forty feet per second to one hundred eighty feet per second. After reaching the maximum speed, the air speed was reduced to the minimum value in small increments. Around fifteen data points were taken for each test.

After installing the dummy system, the test was repeated. The soft skin airfoil was tested following the same procedures. The procedures for vacuum control inside the airfoil was the same as in tunnel II.

CHAPTER VII

EXPERIMENTAL RESULTS

The test data were divided into two groups. Group 1 data were taken from tunnel I and Group 2 data resulted from the use of tunnel II.

Group 1

As defined before,

$$C_D = \frac{D}{\frac{1}{2}\rho V^2 \cdot A}$$

where D was determined by using Figure 6-7 , and the strain gage reading and V was determined by using Figure 6-2 , and the manometer reading. C_D was found for every different velocity and corresponding drag force.

The drag coefficient of NACA 0012 and 0006 (22) along with the Prandtl turbulent drag coefficient and Blasius laminar drag coefficient for a flat plate are presented with data for hard surface 0009 airfoil obtained from tunnel I in Figure 7-1 Obviously the values for 0009 airfoil are too high. The reason for these higher values is mainly due to the interference drag of the ends of the airfoil adjacent to the

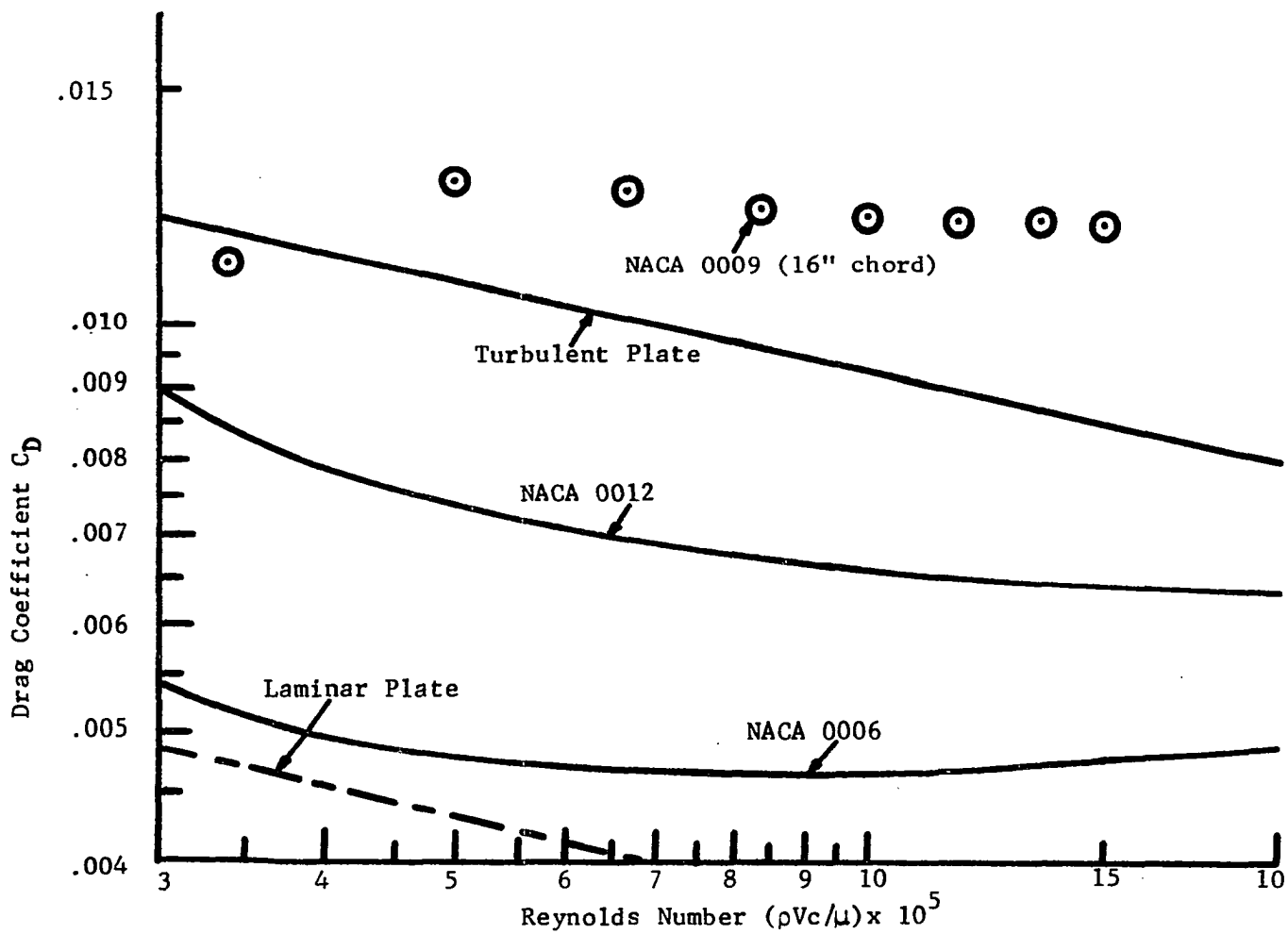

Figure 7-1. Skin-Friction Drag Coefficient for Different Airfoils

ceiling and the floor of the test section. Figure 7-2 indicates the different drag coefficient values for thicknesses of .0025 and .0001 inch PVC skin airfoil and the hard surface airfoil. Figure 7-3, shows the relative percentage amount of skin friction drag reduction of different skins of airfoils.

Group II

To obtain the section drag, the parasitic drag originating at the ends must be subtracted from the readings of the wind-tunnel balance. The wing-tip drag is obviously a function of the profile dimensions at the tips. The drag coefficient of this component is, therefore, based on the tip area. Various investigations of the wing, concurrently tested with rounded and with blunt lateral edges, have been evaluated (22). Results have also been obtained by comparing force tests (with blunt ends) to wake-survey results. For zero lift, Figure 7-4 approximately indicates

$$C_{DC} = 0.15\ (t/c)^2$$

For the forty inch chord NACA 0009 airfoil

$$C_{DC} = .00135$$

In order to eliminate tare-interference drag forces, tests with a dummy wind-shield and supporting strut and tests without dummy wind-shield and supporting struct were conducted.

To find the true drag coefficient for the airfoil, both C_{DC} and

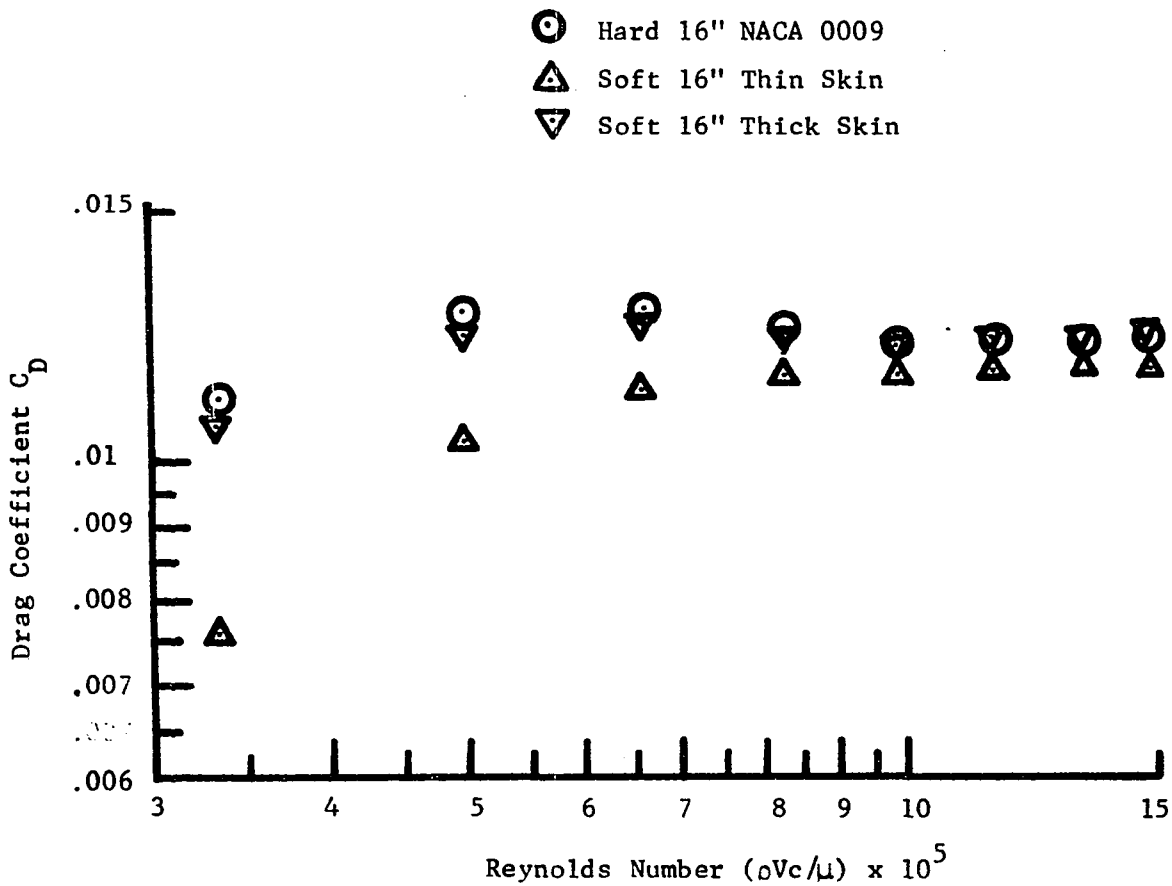

Figure 7-2. Drag Coefficient for Different Airfoils

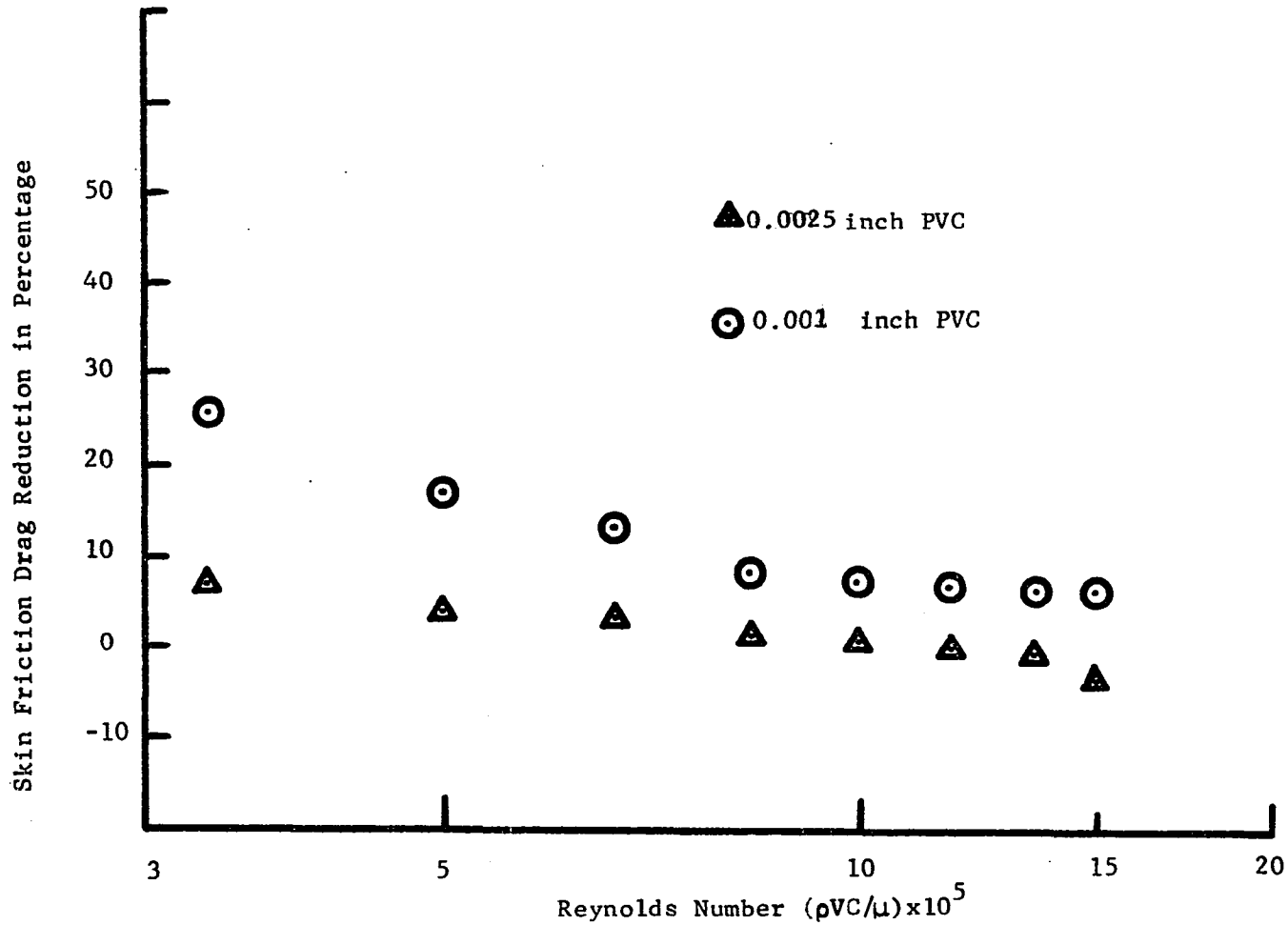

Rigure 7-3. Drag Reduction for 16" NACA 0009 Compliant Coating Airfoil.

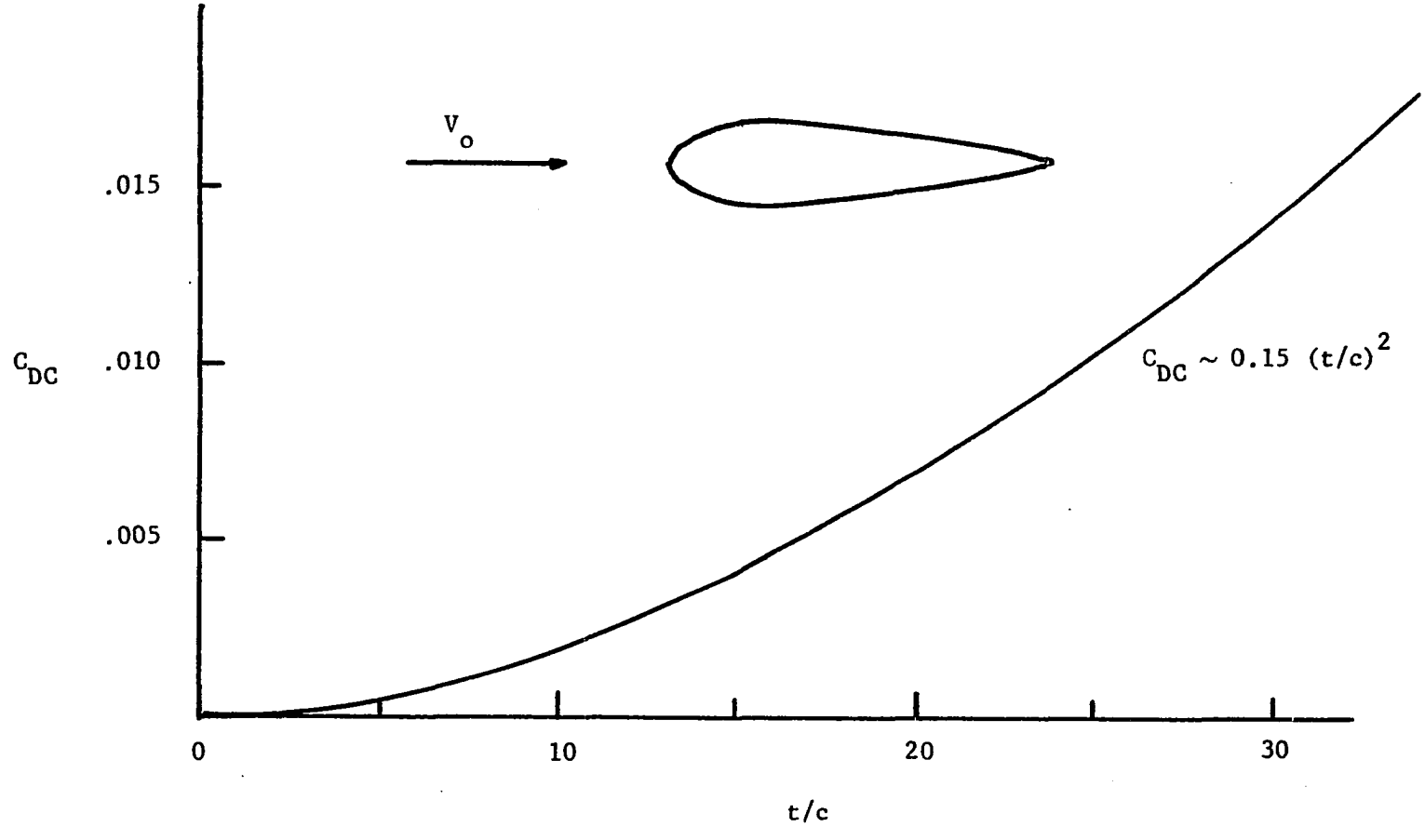

Figure 7-4. Parasite Drag due to Square on Blunt Lateral Edges of Rectangular Wing Models, at Zero Lift. (Reynolds number above 10^6) Ref. Hoerner-(22).

the tare-interference drag must be subtracted from the wind-tunnel test readings.

The procedure for data reduction is much more complicated for tunnel II than tunnel I. The author decided to use the IBM computer to do the job. A program not only to reduce the data but also to plot the points for Figure 7-5 and 7-6 was written (Appendix B).

Figures 7-5 and 7-6, give the drag coefficient for the different arrangements of compliant coating airfoils. These data give the drag coefficient of the airfoils with and without tare and interferences. Figure 7-7 shows the drag coefficient of sectional airfoils with the tare and interferences subtracted out. Figure 7-8 shows the percentage drag reduction for different arrangements of the airfoil below hard plate values. Figures 7-9 and 7-10 show drag reductions for both 16 and 40 inch chord airfoils.

Hoerner (22) indicates that the drag coefficient for NACA 0009 airfoil (hard surface) should be approximately 0.0075 in this Reynolds number range. The difference between this value and the hard surface value of Figure 7-7 is believed to be due to the experimental uncertainties of these tests. This is discussed in Appendix A.

Theory and Discussion

The analysis outlined in Benjamin's report (9) indicated that laminar incompressible, ideal and low disturbance flow could be stabilized (the transition from laminar to turbulent boundary

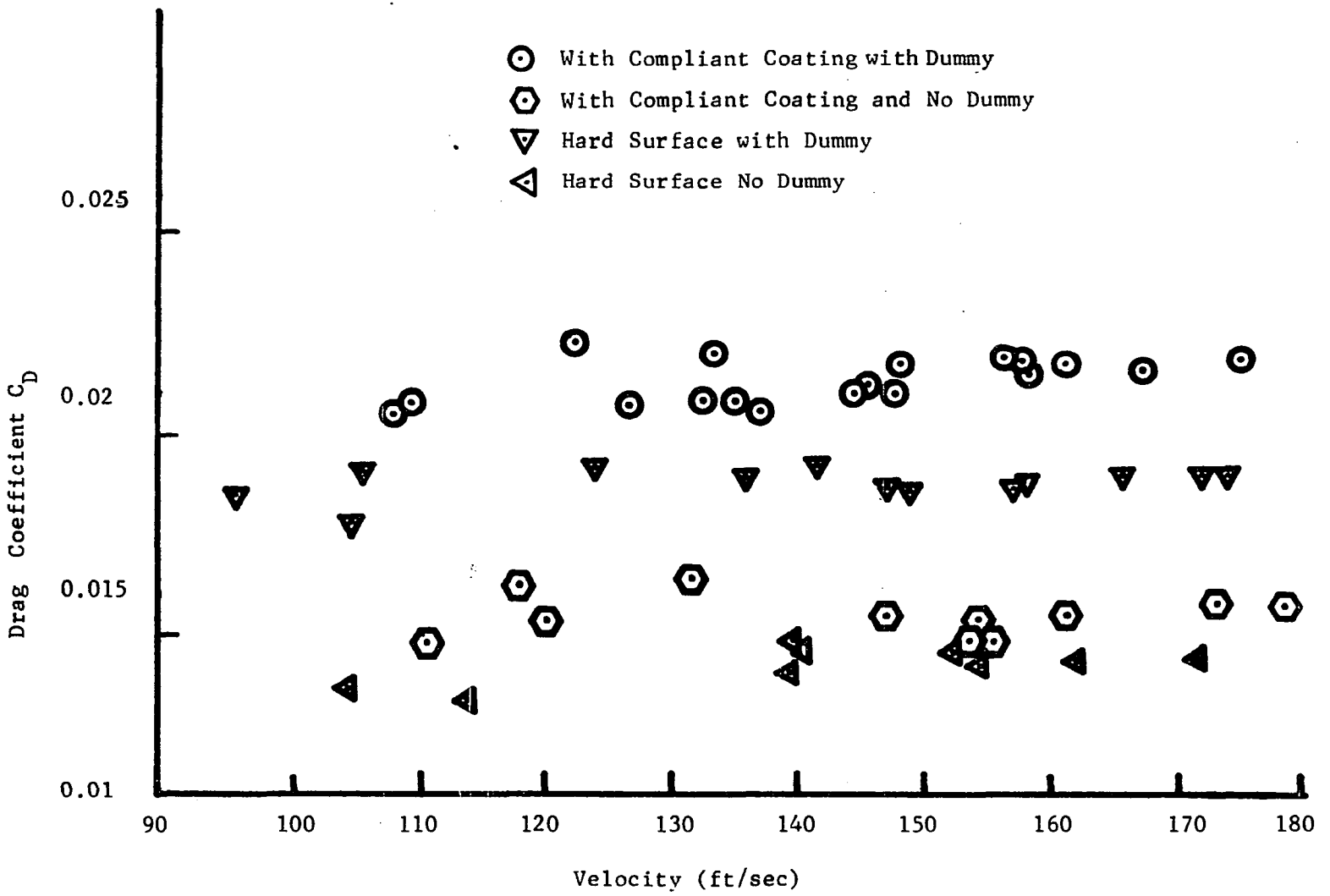

Figure 7-5. Drag Coefficient for .0025 PVC skin 40" Chord NACA 0009 Airfoil.

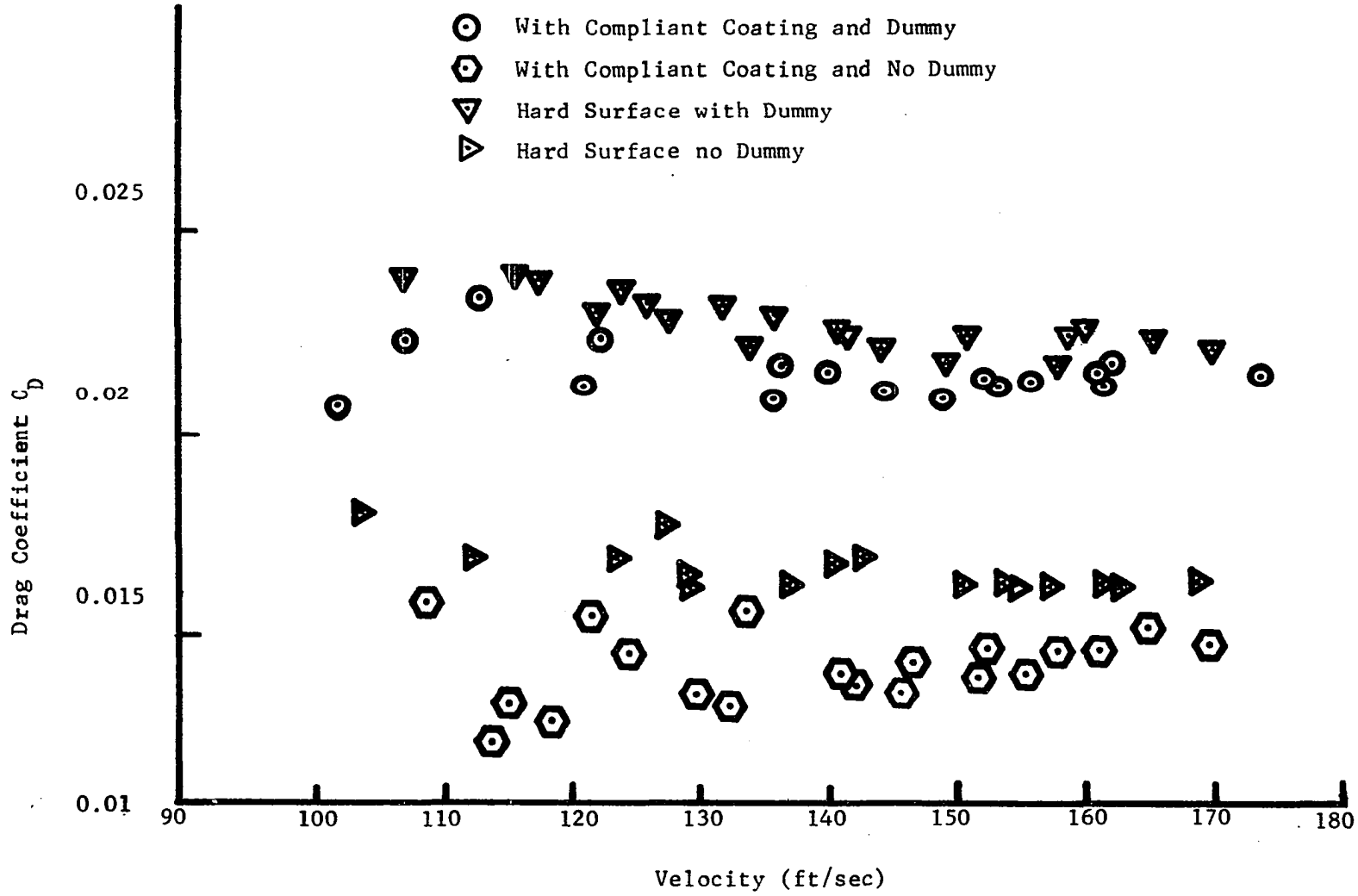

Figure 7-6. Drag Coefficients for .0015 PVC Skin 40" Chord NACA 0009 Airfoil.

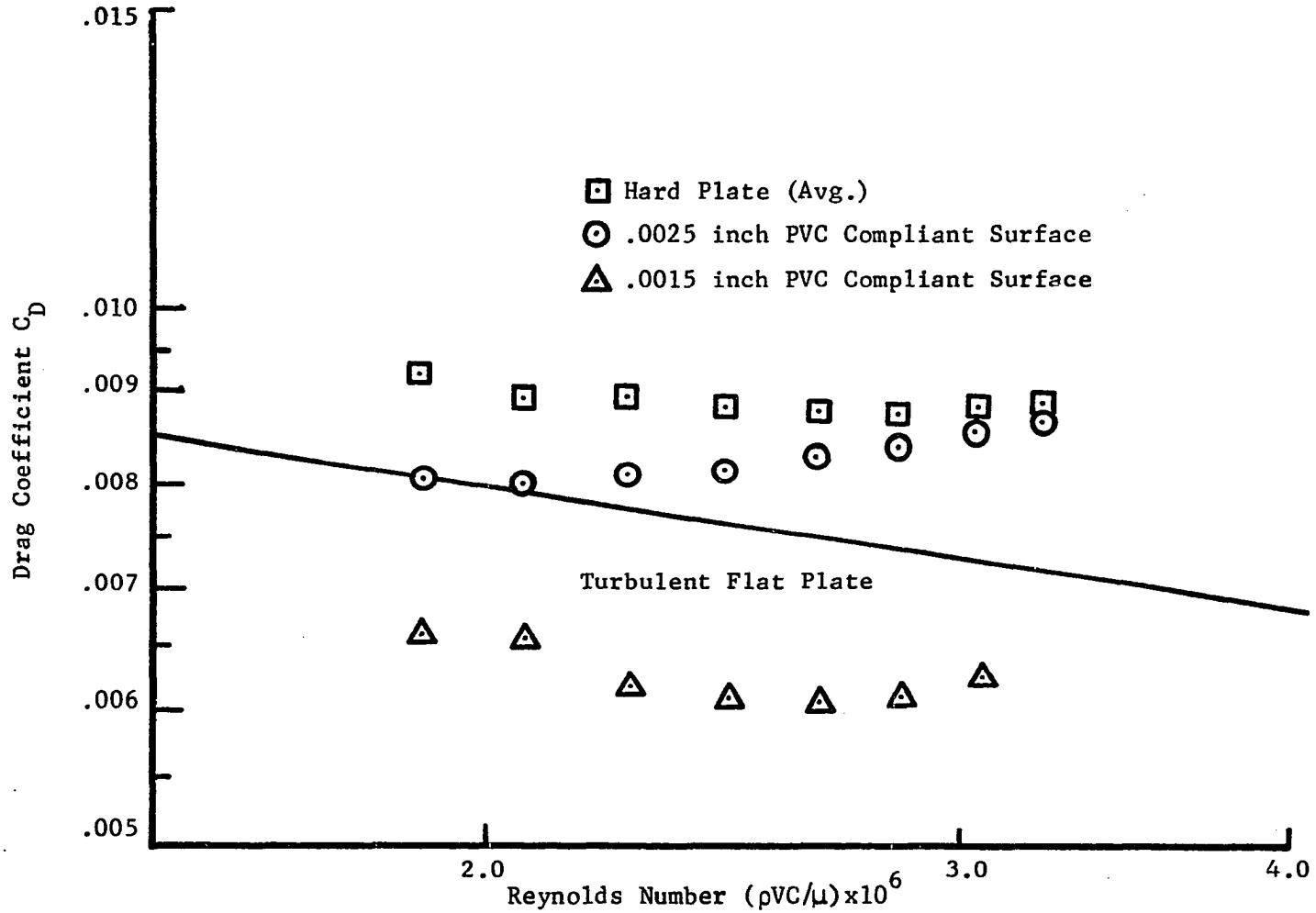

Figure 7-7. NACA 0009 40" Chord Airfoil Drag Coefficient

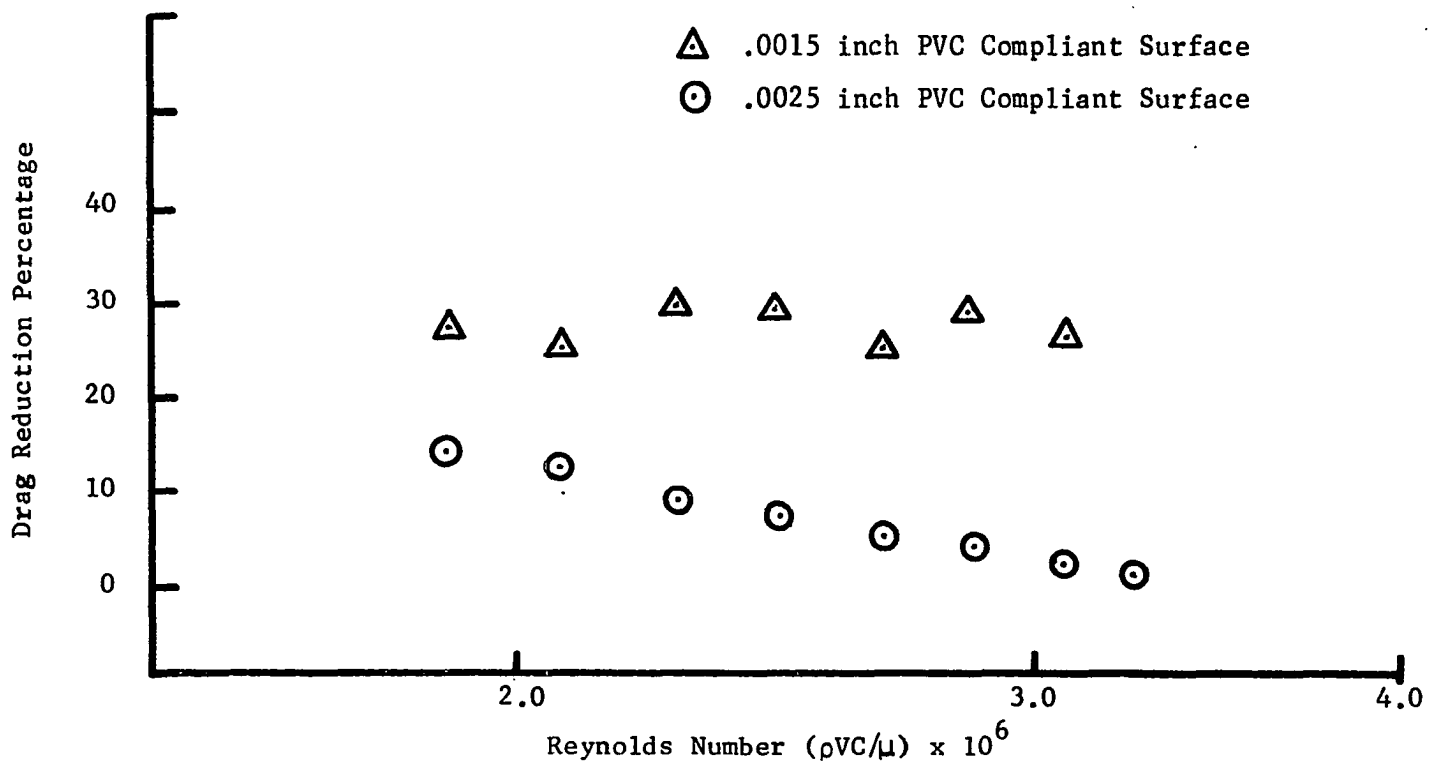

Figure 7-8. Per Cent Drag Reduction Below Hard Plate Values

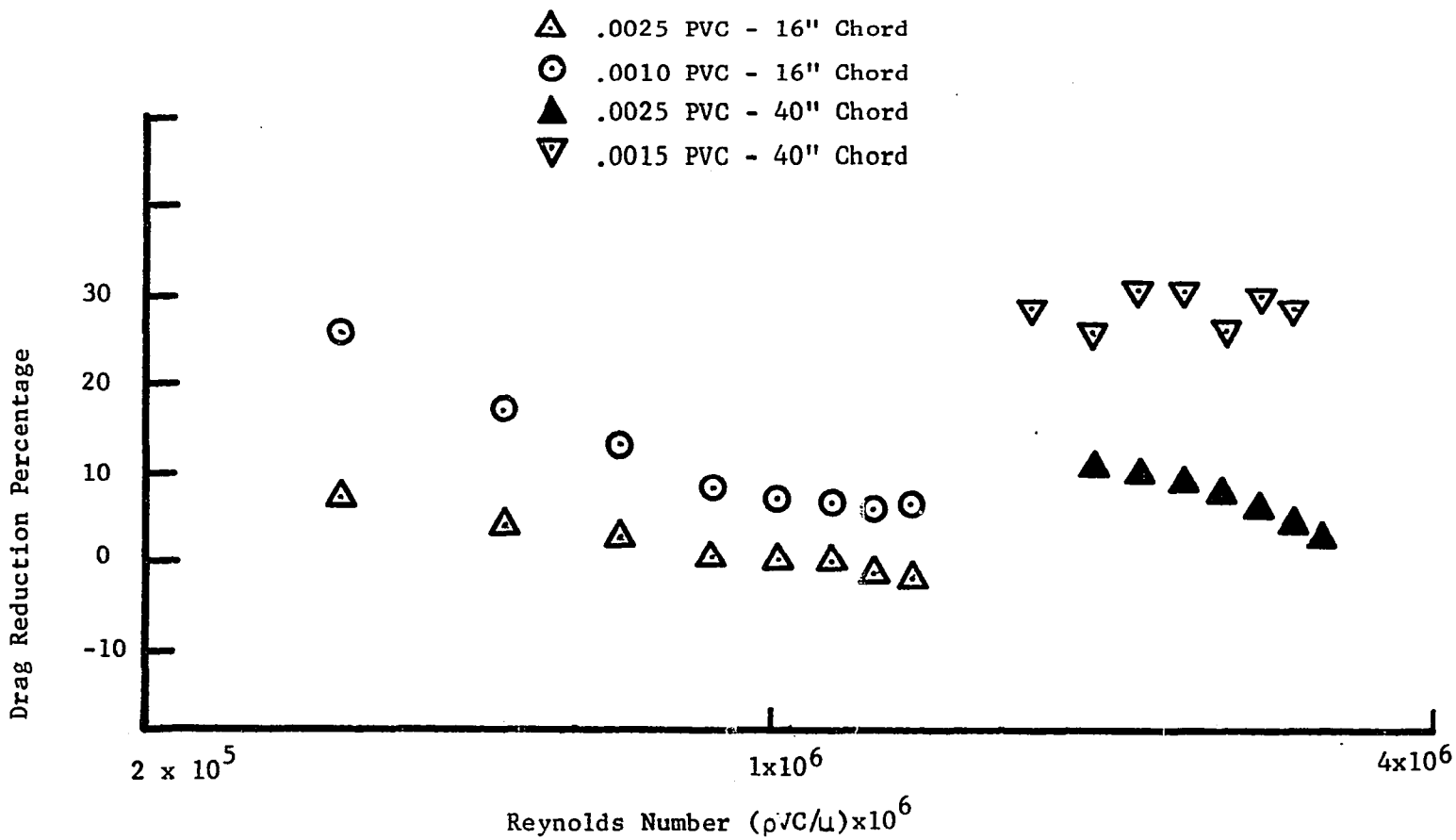

Figure 7-9. Comparison of Drag Reduction for 16" and 40" NACA 0009 Airfoil.

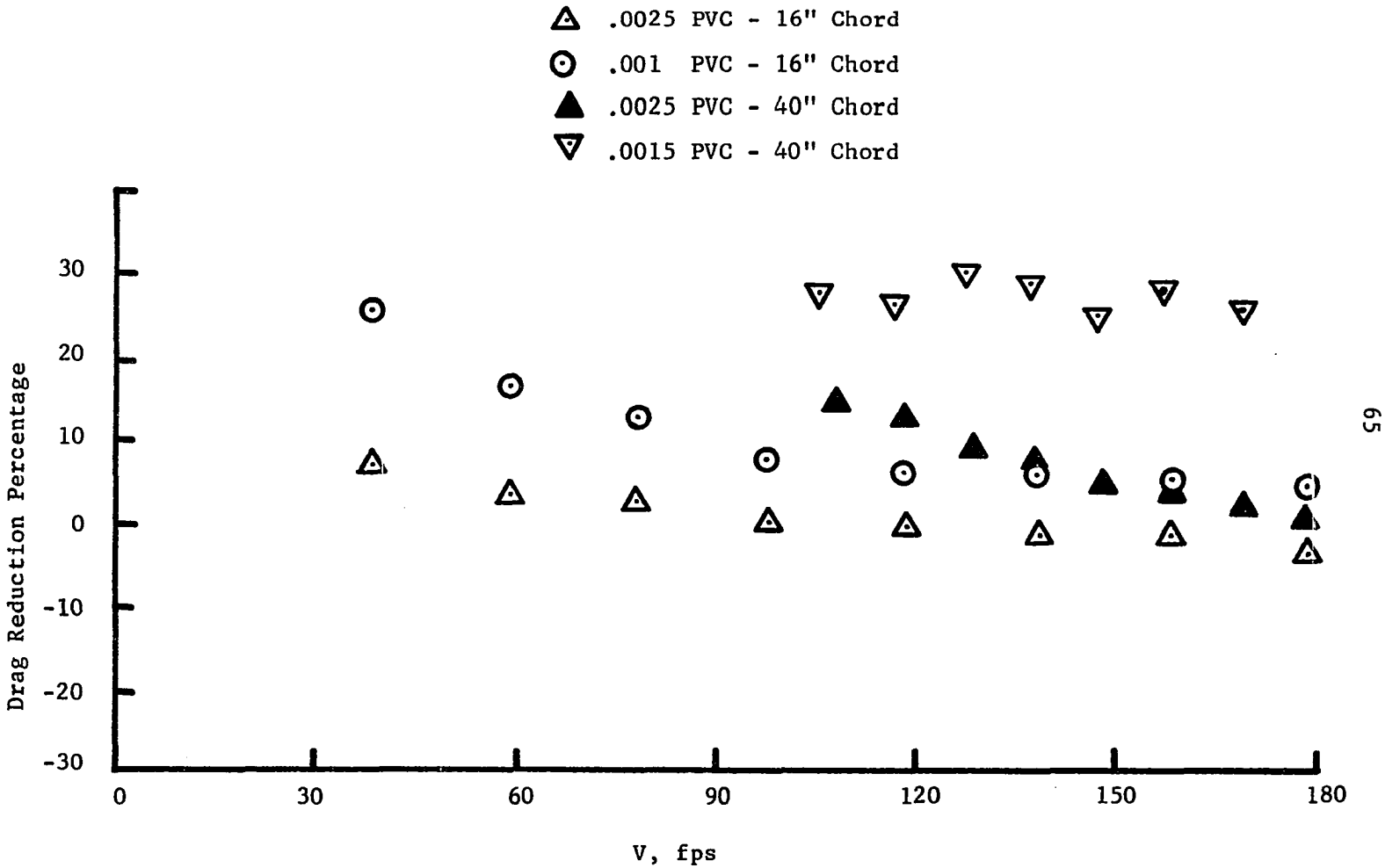

Figure 7-10. Drag Reduction vs Speed

layer could be delayed, by the presence of an ideally designed compliant boundary. As a result skin-friction could be reduced. According to this theory the membrane should be fairly stiff and the damping should be moderate. Kramer's (2,3,4) model has the best result (lowest drag) with moderately high wall damping and fairly stiff membrane, It seems, therefore unlikely that the reported success of Kramer's experiments could be explained on the basis of the simple stability theory alone. The most likely alternative explanation is that the flexible surface has an effect on the fully developed turbulent boundary layer.

Karplus (8), investigating the scale and degree of turbulence for water flow over mylar film with various fluid substrates, concluded that turbulence occurred sooner for the flexible wall than for the solid wall but was retarded in its rate of development. The same conclusion was obtained by Walter's report (16). By using a hot-wire anemometer, a detailed study was made to determine the basic characteristics of the turbulent boundary layer flow with a zero pressure gradient over a compliant surface. The compliant surface was made of a 0.001 inch PVC and 3/16 inch 40 PPI polyurethane foam. The tests were run at a constant velocity of 50 fps. This study over the compliant surface revealed a reduction of turbulent intensities and a 25 per cent decrease in Reynolds stress when compared with hard plate data. These two experiments, clearly show that the secret for compliant coating drag reduction does not depend on the delay of transition but on the complex interaction between the compliant surface and the tur-

bulent boundary layer.

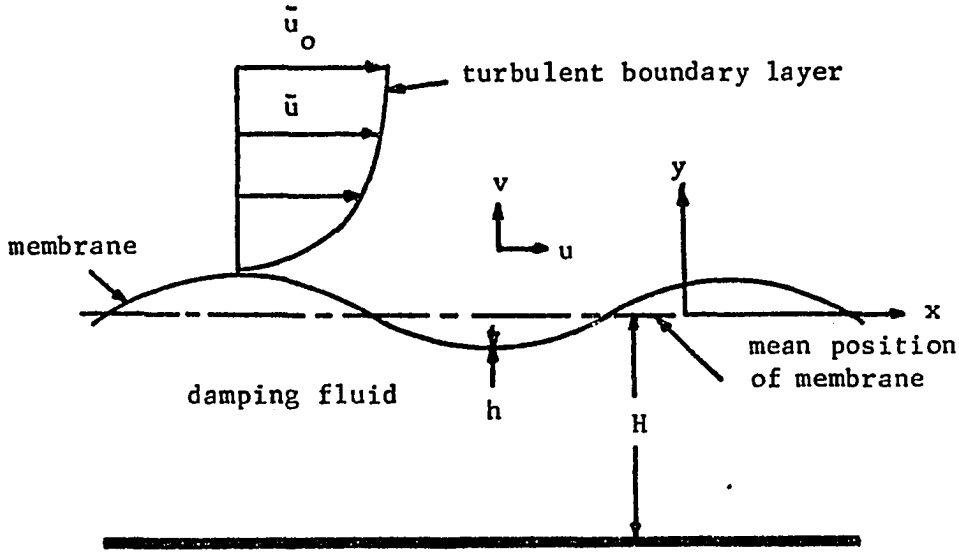

Figure (7-11) Model of the Compliant Coating

A new theory is needed to explain this phenomena. Using a two dimensional model, restricting the motion of the coating in x and y plane only, (Figure 7-11) Blick (11), derived the following expression,

$$\tau = .707 \int_{-\infty}^{\infty} \int_{-\infty}^{\infty} \sqrt{\frac{\omega K^2}{\nu}}\, y\, S_p(K,\omega)\, \frac{[\sigma\omega^2 - TK^2 - DK^4 - \rho g + G_r - G_i]}{[(\sigma\omega^2 - TK^2 - DK^4 - \rho g + G_r)^2 + G_i^2]}\, dK d\omega \quad (7\text{-}1)$$

where τ is the Reynolds stress ($-\rho\ \overline{u'v'}$) induced by the compliant coating in a thin layer adjacent to the coating. It is interesting to notice that all terms in Equation 7-1 are positive except the numerator, which may be positive or negative depends on values for σ, T, D, ρ, ν. These variables can be tuned to find a negative resonant peaks. A negative Reynolds stress might possibly reduce the

total Reynolds stress throughout the boundary layer, thus causing a reduction in wall skin friction. By examining the term in the numerator of equation 7-1. , Table 7-1 was arranged.

Table 7-1. Effect of Compliant Coating on Sign of Perturbation Reynolds Stress (Ref. 11).

Increasing Variable	Perturbation Reynolds Stress	
	Increase	Decrease
Skin mass/Unit area, σ	X	
Skin flexure stiffness, D		X
Skin tension, T		X
Damping fluid density, ρ		X
Fluid layer thickness, * H	X	
Damping fluid kinematic viscosity, * ν		X

* The term $(G_r - G_i)$ was found to increase with H and decrease with ν, Reference (11).

A correlation was found to exist with the variations of σ, T, ρ, and ν over the limited range tested by Looney and Blick (15). Looney and Blick found in their experiments that the skin friction increased with increase in σ, but decreased with an increase in T, ρ, or ν. Hence the limited experimental evidence shows the same trends as predicted by this simplified model of turbulent flow over a compliant surface.

The sucess of Blick, Smith and Looney lead the author to use 40 PPI polyurethane foam as the damping medium.

During Walter's (16) preliminary tests, no reduction of turbulence intensity was found by using a small (approximately 2'x2') compliant coating plate. Later by using the same material (.001 PVC and 40 PPI Polyurethane foam) and a large test plate of 14 foot long by 2 foot wide a 25 percent decrease in the Reynolds stress was recorded. The author suspects that there is a correlation between the thickness of PVC and the longitudinal dimension of the testing model. Using the data presented in Figure 7-10 and a dimensionless variable t^* (t^* = PVC thickness/chord) Figure 7-12 was prepared. The correlation between t^* and drag reduction is apparent. This is very encouraging because it indicates thicker PVC skins can be used for larger airfoils.

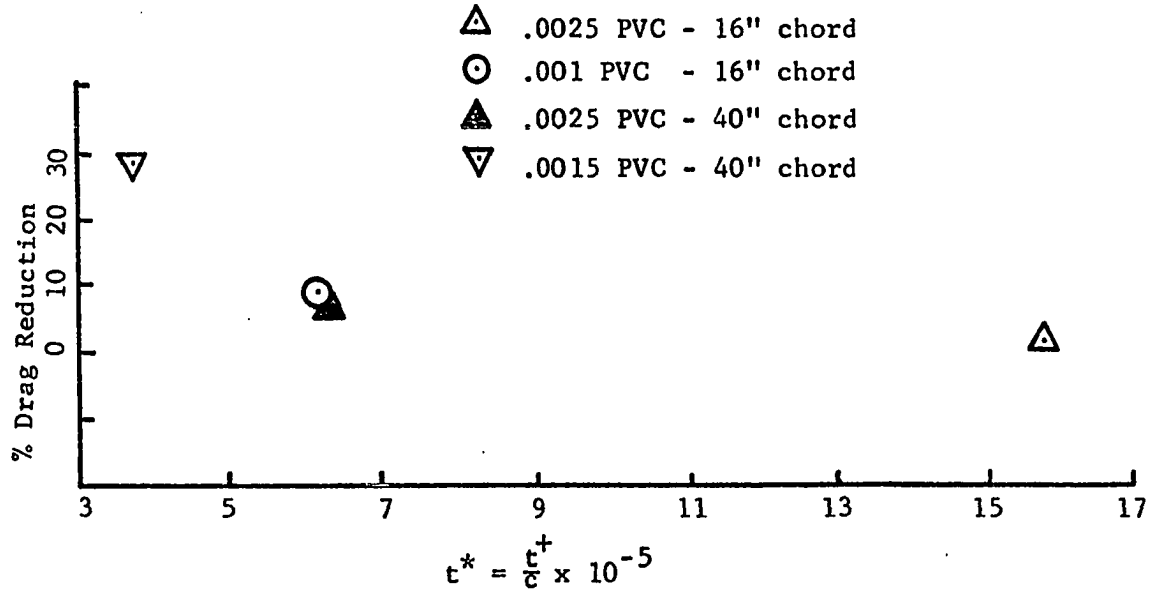

Figure 7-12. Drag reduction verses t^* (these values are the approximate average reduction for the particular PVC and airfoil from Figure 7-10).

The basic construction for Blick's model is composed of a thin membrane stretched over a reservoir containing fluid. Unfortunately this is a very fragile structure. A more rigid structure can be constructed by using a PVC membrane stretched over polyurethane foam. The complete theory (similar to Equation 7-1) has not been derived for the PVC-Polyurethane coating. The main purpose of the fluid under the membrane is for damping and changing the phase angle between u' and v' to near zero degrees. Careful selection of the polyurethane foam could serve the same purpose. Different types of polyurethane foam were tested by Smith and Blick. The result can be seen in Table 1-1. The best result was obtained by using 40 PPI polyurethane foam. From Table 7-2 it is obvious that 40 PPI polyurethane foam by far is the softest and is the heaviest of the tested foams.

Table 7-2. Properties of the Residient Test Material (Ref. 17)

Material	Thickness (in)	Density lb/ft^3	Compression modulus psi
27-PPI polyurethanefoam	31/32	1.6	3.8
40-PPI polyurethane foam	5/32	1.8	0.37
80-PPI polyurethane foam	15/16	1.7	2.52
Foam rubber	5/8	7.6	7.93

PPI = pores/inch

These properties (highest density and damping) again correlate the properties listed in Table 7.1.

CHAPTER VIII

CONCLUSIONS

Several definite conclusions may be made from the experimental study of the compliant surface airfoil at zero incident angle.

1. The results of the compliant coating airfoils plotted in Chapter VII indicate clearly that the drag coefficient of an airfoil is a function of the compliancy of the coating. The thinner PVC skin has higher drag reduction for both tunnel I and tunnel II.

2. Drag coefficient reduction is a function of t^* as shown in Figure 7-12.

3. The tests conducted covered a very wide range of velocity (40 ft/sec to 180 ft/sec) and Reynolds number ($3x10^5$ to $4x10^6$). It is interesting to note that at lower Reynolds number the percentage drag coefficient reduction is higher and at higher Reynolds number the drag coefficient reduction approaches a constant value. The same phenomena was noticed by Boyce and Blick (23) for dusty air flow.

4. Figure 6-3 indicates an apparent jump of data points around Reynolds number 1.5×10^6. This is mainly due to a. The different testing condition. These data were obtained from two tunnels

Tunnel I has a relatively small test section. Choking and side wall interference with testing model were apparent. b. Looney and Blick (15) reported that the higher the longitudinal tension applied on the PVC the more reduction of drag coefficient was measured. Unfortunately the present model airfoil does not allow the precise measurement of longitudinal tension applied on the PVC. No way to determine if tension was the same for the small and large models. This might be another important reason for the jump.

5. Figure 7-10 shows the relationship between drag coefficient reduction and the free stream velocity. Here the general trend of the drag coefficient reduction is more apparent. At low velocity the drag coefficient reduction is higher and as the velocity increases, the reduction approaches a constant value.

6. The china-clay method shows again, that the drag reduction is not caused by the shifting of the transition point. It is caused by the reduced turbulent intensity as indicated by Blick and Walter (16). While conducting the china-clay experiment, the author observed that it took a longer period of time to have the china-clay coating return to white at the rear portion of the compliant airfoil than the hard surface airfoil. This is another indication that the turbulence intensity for the compliant coating airfoil is lower than the corresponding solid airfoil.

Recommendations for Furture Research

In order to gain further insight into the characteristics

of turbulent flow over a compliant surfaced airfoil, additional investigations are needed.

1. Up to now no test has been conducted to investigate the effect of thickness of damping material. Extensive measurements should be conducted in this area.

2. A new airfoil model on which the longitudinal tension can be measured should be tested.

3. No airplane can fly at constant zero incident angle. A series of tests should therefore be conducted to investigate the drag and lift characteristics of the compliant coating wing at angle of attack.

REFERENCES

1. Schlicting, H., "Boundary Layer Theory," 4th Ed., McGraw-Hill, New York, 1960.

2. Kramer, M.O., "Boundary Layer Stabilization by Distributed Damping", Readers Forum, Journal of the Aerospace Sciences, Vol. 27 (1960), p. 68.

3. Kramer, M.P., "Boundary Layer Stabilization by Distributed Damping," Journal of American Society of Naval Engineers, Vol. 72, February, 1960, p. 25-33.

4. Kramer, M.O., "The Dolphin's Secret", Journal of the American Society of Naval Engineers, Vol. 73, February, 1961, pp. 103-107.

5. Laufer, J. and Maestrello, L., "The Turbulent Boundary Layer over a Flexible Surface," Boeing Co., Transport Div., Document D6-9408, December, 1965.

6. Ritter, H. and Messum, L.T., "Water Tunnel Measurements of Turbulent Skin Friction on Six Different Compliant Surfaces of 1 ft. Length", Admiralty Res. Lab., ARL/N4/GHY/9/7, ARL/G/N9, June 1964.

7. Pelt, R., "A Preliminary Investigation of Surface Damping Effects on Fluid Flow Through Flexible Tubes," Ph.D. Dissertation, Department of Chemical Engineering University of Pittsburgh (1964).

8. Karplus, Henry B., "Turbulent Flow Transition Near Solid and Flexible Boundaries," IIT Research Institute, Report No. IITRI 1205-4, 1963.

9. Benjamin, T. Brooke, "Fluid Flow with Flexible Boundaries," Eleventh International Congress of Applied Mechanics, Munich, Germany, 1964.

10. Gregory, N. and Love, Edna M., "Progress Report on an Experiment of the Effect of Surface Flexibility on the Stability of Laminar Flow," Aeronautical Research Council Current Papers, C.P. No. 602, Ministry of Aviation, London, England, 1962.

11. Blick. E.F., "The Theory of Skin Friction Reduction by a Compliant Coating in a Turbulent Boundary Layer," Symposium on Viscous Drag Reduction, Sept. 24-25, 1968, LTV Research Center, Dallas, Texas. Proceedings to be published by Plenum Press.

12. Blick, E.F., Walters. Smith, R., and Chu, H. "Compliant Coating Skin-Friction Experiments," AIAA, Paper No. 69-165.

13. Chu, H.H. and Blick, E.F., "Compliant Surface Drag as a Function of Speed", Journal of Spacecraft and Rockets, Volume 6, Number 6, June 1969.

14. Fisher, D.H. and Blick, E.F., "Turbulent Damping by Flabby Skins," Journal of Aircraft, Vol. 3, No. 2, March-April, 1966, pp. 163-164.

15. Looney, R.W., and Blick, E.F., "Skin Friction Coefficients of Compliant Surfaces in Turbulent Flow," Journal of Spacecraft and Rockets, No. 3, October, 1966, pp. 1562-1564.

16. Walters, R.R. and Blick, E.F., "Turbulent Boundary-Layer Characteristics of Compliant Surfaces," Journal of Aircraft, Volume 5, No. 1, January-February 1968, pp. 11-16.

17. Smith, R. and Blick, E.F., "Experimental Turbulent Skin Friction Coefficients of Compliant Surfaces on Flat Plates", University of Oklahoma, Oklahoma 1968.

18. UBEROI, U.S., "Effect of Wind-Tunnel Contraction on Free-Stream Turbulence", Journal of Aeronautical Sciences, Vol. 23, August, 1956, pp. 754-764.

19. Comp, L.A., "Laboratory Manual for Wind-Tunnel Testing", University of Oklahoma, Norman, Oklahoma, 1964.

20. Pope, A., "Wind-Tunnel Testing," Ed. 2, New York: John Wiley and Sons, Inc., 1961.

21. Abbott, I.H. and Von Doenhoff "Theory of Wing Sections", Dover Publications, Inc., New York, 1959.

22. Hoerner, S.F., "Fluid-Dynamic Drag", Published by the Author, 1965.

23. Boyce, M.P. and Blick, E.F., "Fluid Flow Phenomena in Dusty Air", Journal of Basic Engineering, Vol. 92, Series D, No. 3, September 1970, pp. 495-503.

APPENDIX A

ERROR CONSIDERATIONS

ERROR CONSIDERATIONS

Error is inherent in any experimental project, but more specifically this error may be thought of as experimental uncertainty. The following expression

$$\Delta C_D = [(\Delta C_{D_1})^2 + (\Delta C_{D_2})^2 + \ldots (\Delta C_{D_i})^2]^{\frac{1}{2}}$$

where

C_D = overall uncertainty in drag coefficients

C_i = maximum error involved in primary measurements

estimates this uncertainty, based on the uncertainties in the primary measurements.

The strain gage indicator reading accuracy for the drag force is estimated at $\pm$ 2.0 micro-inches/inch for tunnel I and $\pm$ 0.5 micro-inches/inch for tunnel II. Force deviations may be seen in Tables A-1 and A-2.

Vibrations and mechanical friction in the balance system of tunnel II were observed and to cause deviations estimated at .5 micro-inches/inch.

The accuracy of the pressure readings for velocity is estimated for tunnels I and II to be $\pm$ 0.02 inches of red oil (S.G. 0.827) and water respectively. These velocity deviations are shown in Tables A-4 and A-5.

The strain converter and the strain indicator are also estimated to have an accuracy of $\pm$ 0.00833 micro-inches and $\pm$ 0.125 micro-inches respectively. The corresponding errors are 4.8×10^{-7} and 7.5×10^{-6}. Since these errors are negligible in the final calculations for expected uncertainty, they were allowed to remain constant, even though they should deviate with velocity.

The percentage of uncertainty includes the force and velocity deviations for both the hard and soft airfoils. They were calculated as follows:

$$\Delta C_D = [(\Delta C_{DF})^2 + (\Delta C_{DM})^2 + (\Delta C_{DSC})^2 + (\Delta C_{DSI})^2 + (\Delta C_{DV})^2]^{\frac{1}{2}}$$

$$\text{The expected uncertainty in per cent} = \frac{\Delta C_D \times 100}{C_{D_{original}}}$$

The combined uncertainty for the difference between hard and soft in tunnel II were then calculated by

$$C_{DE} = [(\Delta C_{D_{soft}})^2 + (\Delta C_{D_{hard}})^2]^{\frac{1}{2}}$$

and the results are illustrated in Tables A-6 and A-7.

TABLE A-1

FORCE DEVIATIONS (TUNNEL I)

Velocity(ft/sec)	29	66	92	121	180	189
$\Delta C_{DF} \times 10^{-4}$	± 3.875	± 2.89	$+1.542$	± 0.892	± 0.58	± 0.364

TABLE A-2

FORCE DEVIATIONS (TUNNEL II)

Velocity (ft/sec)	110	130	150	170
$\Delta C_{DF} \times 10^{-4}$	± 4.35	± 3.11	± 2.34	± 1.82

TABLE A-3

MECHANICAL FRICTION DEVIATIONS (TUNNEL II)

Velocity (ft/sec)	110	130	150	170
$\Delta C_{DM} \times 10^{-4}$	± 4.35	± 3.11	± 2.34	± 1.82

TABLE A-4

VELOCITY DEVIATIONS (TUNNEL II)

Velocity (ft/sec)	29	66	92	121	150	189
$\Delta C_{DV} \times 10^{-4}$	± 2.0	± 0.7	± 0.6	± 0.6	± 0.4	± 0.4

TABLE A-5

VELOCITY DEVIATIONS (TUNNEL II)

Velocity (ft/sec)		110	130	150	170
$\Delta C_{DV} \times 10^{-4}$	Hard	+0.3	+0.5	+0.5	+0.8
		-1.1	-0.4	-0.1	-0.3
	Soft	+0.5	+0.7	+0.6	+0.2
		-0.4	-0.3	-0.4	-0.3

TABLE A-6

EXPECTED UNCERTAINTY (TUNNEL I)

Velocity (ft/sec)	29	66	92	121	150	189
C_{DE}	$\pm$3.52%	$\pm$2.29%	$\pm$1.38%	$\pm$0.93%	$\pm$0.198%	$\pm$0.156%

TABLE A-7

EXPECTED UNCERTAINTY (TUNNEL II)

Velocity (ft/sec)	110	130	150	170
C_{DE}	+8.74%	+5.95%	+4.74%	+3.78%
	-8.8 %	-5.94%	-4.69%	-2.7 %

APPENDIX B

COMPUTER PROGRAM FOR DATA DEDUCTION

```
PAGE    1     ER020801

// JOB T                                                ER020801    075401     H CHU

LOG DRIVE    CART SPEC    CART AVAIL   PHY DRIVE
  0000         0C01         0C01         0000

V2 M09    ACTUAL  8K  CONFIG  8K

// FOR
** ER020801,HUMPHREY CHU,ASME599
*ONE WORD INTEGERS
*EXTENDED PRECISION
*LIST SOURCE PROGRAM
PAGE    2     ER020801    ER020801,HUMPHREY CHU,ASME599

C   THIS SUB-PROGRAM  PLOTS THE POINTS ON THE X AND Y AXIS
       COMMON     X(4,25),Y(4,25),AI(4,77),JX(4),MX(5),CCC(4,10),IX,XMAG
       SX=.075*XMAG
       SY=240.*XMAG
       CALL SCALE(SX,SY,90.,.005)
       DO 4001 I=1,IX
       IR=I-1
       NUMB=JX(I)
       DO 4002 J=1,NUMB
       XP=X(I,J)
       YP=Y(I,J)
       CALL EPLOT(-2,XP,YP)
       CALL POINT(IR)
       CALL EPLOT(1,XP,YP)
4002   CONTINUE
       DO 4003 J=1,181
       RJ=J
       MXX=MX(I)+1
       YP=CCC(I,1)
       XP=175.5-.5*RJ
```

```
      DO 4004 K=2,MXX
4004  YP=YP+CCC(I,K)*XP**(K-1)
      IF(YP-.03) 4005,4007,4007
4005  IF(YP-.005) 4007,4007,4006
4007  IP=1
      GO TO 4003
4006  CALL EPLOT(IP,XP,YP)
      IP=2
4003  CONTINUE
      CALL EPLOT(1,90.,.005)
4001  CONTINUE
      CALL EPLOT(1,90.,.005)
      CALL EPLOT(-2,82.,.005)
      CALL POINT(1)
      CALL EPLOT(1,90.,.005)
      CALL EXIT
      END

FEATURES SUPPORTED
 ONE WORD INTEGERS
 EXTENDED PRECISION

CORE REQUIREMENTS FOR
 COMMON    1658  VARIABLES      30  PROGRAM     262

END OF COMPILATION

// DUP

*STORE       WS  UA  DRAW
CART ID 0C01    DB ADDR  45D8    DB CNT   0012

C  THIS SUB-PROGRAM  PLOTS THE X AND Y AXIS
      COMMON    X(4,25),Y(4,25),AI(4,77),JX(4),MX(5),CCC(4,10),IX,XMAG
11    FORMAT(I3,1X,77A1)
3011  FORMAT (F4.0)
3012  FORMAT (F5.3)
3013  FORMAT     (14HVELOCITY (FPS))
```

```
3014  FORMAT (16HDRAG COEFFICIENT)
      XMAG=2.
      SX=.075*XMAG
      SY=240.*XMAG
      SNX=.09*XMAG
      SNY=.15*XMAG
      SLX=.18*XMAG
      SLY=.30*XMAG
      CALL SCALE(SX,SY,90.,.005)
      CALL EPLOT(-2,82.,.005)
      CALL POINT(1)
      CALL EPLOT(1,90.,.005)
      CALL EGRID(0,90.,.005,2.,45)
      CALL EGRID(1,90.,.005,.001,25)
      DO 3001 I=1,10
      RI=I
      XNO=80.+10.*RI
      YAX=.00375
      XAX=XNO-2.4*XMAG
      CALL ECHAR(XAX,YAX,SNX,SNY,0.)
3001  WRITE(7,3011) XNO
      DO 3002 I=1,6
      RI=I
      YNO=.005*RI
      XAX=82.8
      YAX=YNO-.0003125
      CALL ECHAR(XAX,YAX,SNX,SNY,0.)
3002  WRITE(7,3012) YNO
      CALL ECHAR(121.,.001875,SLX,SLY,0.)
      WRITE(7,3013)
      CALL ECHAR(81.6,.011,SLX,SLY,1.5708)
      WRITE(7,3014)
      DO 3003 I=1,IX
      RI=I
      IR=I-1
      YAX=.035+SNY*(.5-1.5*RI)/SY
      CALL EPLOT(-2,100.,YAX)
```

```
      CALL POINT(IR)
      CALL ECHAR(103.,YAX,SNX,SNY,0.)
      WRITE(7,11) I,(AI(I,J),J=1,77)
3003  CONTINUE
      CALL EPLOT(1,90.,.005)
      CALL LINK(DRAW)
      END

FEATURES SUPPORTED
 ONE WORD INTEGERS
 EXTENDED PRECISION
 IOCS

CORE REQUIREMENTS FOR
 COMMON    1658  VARIABLES      40  PROGRAM     436

END OF COMPILATION

// DUP

*STORE       WS  UA  GRID
CART ID 0C01    DB ADDR  45ED    DB CNT    001E

// FOR
** ER020801,HUMPHREY CHU,ASME599
*IOCS(1403 PRINTER)
*ONE WORD INTEGERS
*EXTENDED PRECISION
*LIST SOURCE PROGRAM

C   THIS SUB PROGRAM  FITS THE CURVE BY USING LEAST SQUARE METHORD.
      DIMENSION DDEV(10),YYCAL(25),A(10,10),B(10),C(10),CC(10,10),P(20)
      COMMON    X(4,25),Y(4,25),AI(4,77),JX(4),MX(5),CCC(4,10),IX,XMAG
11    FORMAT(1H ,///,I3,5X,77A1,/)
757   FORMAT (I3,5X,E14.7)
755   FORMAT (I3,1X,10(E10.3,1X))
```

```
6001  FORMAT(//)
      DO 1012 LX=1,IX
      NUMB=JX(LX)
      DO 1001  M=1,9
      MX2=M*2
      DO 13 I=1,MX2
      P(I)=0.0
      DO 13 J=1,NUMB
13    P(I)=P(I)+X(LX,J)**I
      N=M+1
      DO 30 I=1,N
      DO 30 J=1,N
      K=I+J-2
      IF(K)29,29,28
28    A(I,J)=P(K)
      GO TO 30
29    A(1,1)=NUMB
30    CONTINUE
      B(I)=0.0
      DO 21 J=1,NUMB
21    B(I)=B(I)+Y(LX,J)
      DO 22 I=2,N
      B(I)=0.0
      DO 22 J=1,NUMB
22    B(I)=B(I)+Y(LX,J)*X(LX,J)**(I-1)
      NMI=N-1
      DO 300 K=1,NMI
      KPI=K+1
      L=K
      DO 400 I=KPI,N
      IF(ABS(A(I,K))-ABS(A(L,K))) 400,400,401
401   L=I
400   CONTINUE
      IF(L-K)500,500,405
405   DO 410 J=K,N
      TEMP=A(K,J)
```

```
      A(K,J)=A(L,J)
410   A(L,J)=TEMP
      TEMP=B(K)
      B(K)=B(L)
      B(L)=TEMP
500   DO 300 I=KPI,N
      FACT=A(I,K)/A(K,K)
      A(I,K)=0.0
      DO 301 J=KPI,N
301   A(I,J)=A(I,J)-FACT*A(K,J)
300   B(I)=B(I)-FACT*B(K)
      C(N)=B(N)/A(N,N)
      I=NMI
710   IP1=I+1
      SUM=0.0
      DO 700 J=IP1,N
700   SUM=SUM+A(I,J)*C(J)
      C(I)=(B(I)-SUM)/A(I,I)
      I=I-1
      IF(I)800,800,710
800   CONTINUE
      DO 900 I=1,N
900   CC(M,I)=C(I)
1001  CONTINUE
      WRITE(5,11) LX,(AI(LX,JR),JR=1,77)
      DO 1002 MY=1,9
      I=MY+1
1002  WRITE(5,755) MY,(CC(MY,J),J=1,I)
      DO 601 I=1,9
      DO 610 J=1,NUMB
      II=I+1
      YCAL=CC(I,1)
      DO 620   K=2,II
620   YCAL=YCAL+CC(I,K)*X(LX,J)**(K-1)
610   YYCAL(J)=YCAL
      DEVV=0.
```

```
      DO 630 K=1,NUMB
630   DEVV=DEVV+(ABS(YYCAL(K)-Y(LX,K))**2)
      DEV=DEVV/NUMB
      WRITE(5,757) I,DEV
601   DDEV(I)=DEV
      STDEV=DDEV(1)
      DO 621 I=1,9
      IF(DDEV(I)-STDEV) 622,622,621
622   STDEV=DDEV(I)
      MDEG=I
621   CONTINUE
      MX(LX)=MDEG
      MM=MDEG+1
      DO 623 J=1,MM
623   CCC(LX,J)=CC(MDEG,J)
      WRITE(5,755) MDEG,(CC(MDEG,I),I=1,MM)
1012  CONTINUE
      DO 1013 M=1,IX
      WRITE(5,11) M,(AI(M,J),J=1,77)
      ID=MX(M)
      IDD=ID+1
      WRITE(5,755) ID,(CCC(M,J),J=1,IDD)
1013  CONTINUE
      WRITE(5,6001)
      CALL LINK(GRID)
      END

FEATURES SUPPORTED
 ONE WORD INTEGERS
 EXTENDED PRECISION
 IOCS

CORE REQUIREMENTS FOR
 COMMON    1658  VARIABLES     874  PROGRAM    1174

END OF COMPILATION
```

```
// DUP

*STORE       WS  UA  FIT
CART ID 0C01    DB ADDR  460B    DB CNT    004E

// FOR
** ER020801,HUMPHREY CHU,ASME599
*IOCS(CARD,1403 PRINTER)
*ONE WORD INTEGERS
*EXTENDED PRECISION
*LIST SOURCE PROGRAM

C   THIS IS THE MAIN PROGRAM  WHICH REDUCES THE EXPERIMENTAL DATA
C   OSGR=ORIGINAL STRAIN GAGE READING
C   AREA=AIRFOIL PROJECTED AREA
C   CBR=CORRECTED BAROMETRIC READING
C   DELP=CHANGE OF STATIC PRESSURE(INCH OF WATER)
C   SGR=STRAIN GAGE READING
C   TEMP=TUNNEL TEST SECTION TEMPERATURE
       COMMON    X(4,25),Y(4,25),AI(4,77),JX(4),MX(5),CCC(4,10),IX,XMAG
C      RE6=RE*10**6
6001   FORMAT(1H1)
10     FORMAT (I3,77A1)
11     FORMAT(1H ,///,I3,5X,77A1,/)
12     FORMAT(1H ,3HNO.,5X,8HVEL(FPS),9X,2HCD,10X,8HDELP(IN),7X,
      1  7HREY.NO.,/)
2      FORMAT (3F15.8)
6      FORMAT(1X,I3,2X,4(E13.6,2X))
3      READ(2,10) IX,(AI(IX,J),J=1,77)
       IF(IX) 5,5,8
8      CONTINUE
       WRITE(5,11) IX,(AI(IX,J),J=1,77)
       READ (2,2) OSGR, AREA,CBR
       WRITE(5,13)
       WRITE(5,2) OSGR,AREA,CBR
13     FORMAT(1H,4HOSGR,11X,4HAREA,11X,3HCBR)
```

```
      WRITE(5,14)
14    FORMAT(1H,4HDELP,11X,3HSGR,12X,4HTEMP)
      WRITE(5,12)
      J=0
1     READ (2,2) DELP, SGR,TEMP
      WRITE(5,2)DELP,SGR,TEMP
      IF(DELP)5,3,4
4     J=J+1
      JX(IX)=J
      DRAG=ABS((OSGR-SGR)*.114)
      RO=CBR*144.*14.7/(29.92*53.35*32.2*(TEMP+460.))
      V2=3.385*DELP*3.385
      V=(V2/RO)**.5
      CD=DRAG/(.5*V2*AREA)
      RE6=(V*3.33)/(160.+(TEMP-68.)*.64)*10.**6
      WRITE(5,6) J,V,CD,DELP,RE6
      X(IX,J)=V
      Y(IX,J)=CD
      GO TO 1
5     CONTINUE
      WRITE(5,6001)
      CALL LINK(FIT)
      END

FEATURES SUPPORTED
 ONE WORD INTEGERS
 EXTENDED PRECISION
 IOCS
CORE REQUIREMENTS FOR
 COMMON    1658  VARIABLES      46  PROGRAM      422

END OF COMPILATION

// XEQ        L
```

1 SOFT 0009 40 THIN WITHOUT DUMMY 6-18-70

OSGR	AREA	CBR
4597.00000381	10.00000000	28.70000001

DELP NO.	VEL(FPS)	SGR CD	TEMP DELP(IN)	REY.NO.
	2.20000000	4579.00000381	93.00000005	
1	0.108599E 03	0.162804E-01	0.220000E 01	0.205475E 07
	2.74000000	4575.00000381	94.00000005	
2	0.121306E 03	0.159767E-01	0.274000E 01	0.228685E 07
	3.32000000	4570.00000381	95.00000005	
3	0.133650E 03	0.161824E-01	0.332000E 01	0.251046E 07
	3.98000000	4567.00000381	96.00000005	
4	0.146464E 03	0.149987E-01	0.398000E 01	0.274127E 07
	4.29000000	4564.00000381	97.00000005	
5	0.152198E 03	0.153064E-01	0.429000E 01	0.283837E 07
	4.80000000	4560.00000381	98.00000005	
6	0.161135E 03	0.153383E-01	0.480000E 01	0.299431E 07
	5.30000000	4555.50000381	99.00000005	
7	0.169471E 03	0.155807E-01	0.530000E 01	0.313801E 07
	4.45000000	4564.00000381	99.00000005	
8	0.155288E 03	0.147560E-01	0.445000E 01	0.287539E 07
	3.71000000	4570.00000381	99.00000005	
9	0.141790E 03	0.144812E-01	0.371000E 01	0.262545E 07
	2.60000000	4579.50000381	99.00000005	
10	0.118698E 03	0.133931E-01	0.260000E 01	0.219788E 07
	2.40000000	4581.50000381	99.00000005	
11	0.114042E 03	0.128510E-01	0.240000E 01	0.211165E 07
	2.85000000	4575.50000381	98.00000005	
12	0.124163E 03	0.150110E-01	0.285000E 01	0.230727E 07
	3.23000000	4574.50000381	98.50000005	
13	0.132241E 03	0.138610E-01	0.323000E 01	0.245300E 07
	3.69000000	4570.00000381	99.00000005	
14	0.141407E 03	0.145597E-01	0.369000E 01	0.261836E 07

```
    4.25000000   4565.50000381     99.50000005
15    0.151826E 03    0.147482E-01    0.425000E 01    0.280630E 07
    4.59000000   4561.50000381    100.00000005
16    0.157853E 03    0.153898E-01    0.459000E 01    0.291252E 07
    5.00000000   4557.00000381    100.50000005
17    0.164826E 03    0.159186E-01    0.500000E 01    0.303579E 07
    3.90000000   4569.00000381    101.00000005
18    0.145635E 03    0.142860E-01    0.390000E 01    0.267759E 07
    3.10000000   4575.00000381    101.00000005
19    0.129842E 03    0.141214E-01    0.310000E 01    0.238722E 07
    2.45000000   4580.00000381    101.00000005
20    0.115429E 03    0.138070E-01    0.245000E 01    0.212224E 07
    0.00000000      0.00000000      0.00000000
```

```
 2      SOFT 0009 40 THIN WITH DUMMY 6-18-70

OSGR              AREA              CBR
 4599.00000381     10.00000000     28.70000001
DELP              SGR               TEMP
NO.       VEL(FPS)          CD             DELP(IN)        REY.NO.

    2.34000000   4571.00000381     96.00000005
  1   0.112304E 03    0.238100E-01    0.234000E 01    0.210193E 07
    2.75000000   4567.50000381     97.00000005
  2   0.121856E 03    0.227926E-01    0.275000E 01    0.227252E 07
    3.60000000   4559.00000381     98.00000005
  3   0.139547E 03    0.221092E-01    0.360000E 01    0.259315E 07
    4.08000000   4555.00000381     98.00000005
  4   0.148559E 03    0.214590E-01    0.408000E 01    0.276062E 07
    4.45000000   4550.00000381    100.00000005
  5   0.155427E 03    0.219105E-01    0.445000E 01    0.286776E 07
```

```
    4.75000000  4546.00000381   100.00000005
 6   0.160581E 03   0.222023E-01   0.475000E 01   0.296285E 07
    2.10000000  4575.00000381    99.50000005
 7   0.106724E 03   0.227409E-01   0.210000E 01   0.197264E 07
    2.68000000  4570.00000381    99.00000005
 8   0.120511E 03   0.215318E-01   0.268000E 01   0.223143E 07
    3.40000000  4561.00000381    99.00000005
 9   0.135737E 03   0.222393E-01   0.340000E 01   0.251337E 07
    3.82000000  4557.50000381   100.00000005
10   0.144005E 03   0.216173E-01   0.382000E 01   0.265701E 07
    4.30000000  4552.00000381   100.50000005
11   0.152853E 03   0.217493E-01   0.430000E 01   0.281528E 07
    4.80000000  4545.00000381   101.00000005
12   0.161568E 03   0.223856E-01   0.480000E 01   0.297052E 07
    5.50000000  4537.50000381   103.00000005
13   0.173256E 03   0.222499E-01   0.550000E 01   0.316306E 07
    4.75000000  4547.00000381   103.00000005
14   0.161010E 03   0.217834E-01   0.475000E 01   0.293950E 07
    4.22000000  4552.50000381   103.00000005
15   0.151762E 03   0.219259E-01   0.422000E 01   0.277066E 07
    3.36000000  4563.00000381   102.50000005
16   0.135358E 03   0.213196E-01   0.336000E 01   0.247552E 07
    1.90000000  4579.00000381   102.00000005
17   0.101741E 03   0.209456E-01   0.190000E 01   0.186399E 07
    0.00000000     0.00000000     0.00000000


 3     HARD 0009 40 THIN WITHOUT DUMMY 6-17-70

OSGR            AREA            CBR
 4644.50000381     10.00000000     28.75000001
DELP            SGR             TEMP
NO.      VEL(FPS)          CD          DELP(IN)       REY.NO.
```

	4.49000000	4606.50000381	92.50000005	
1	0.154940E 03	0.168404E-01	0.449000E 01	0.293688E 07
	4.95000000	4602.50000381	93.50000005	
2	0.162831E 03	0.168834E-01	0.495000E 01	0.307524E 07
	5.50000000	4597.00000381	95.00000005	
3	0.171871E 03	0.171849E-01	0.550000E 01	0.322840E 07
	4.60000000	4605.50000381	95.50000005	
4	0.157252E 03	0.168703E-01	0.460000E 01	0.294847E 07
	3.10000000	4618.00000381	96.00000005	
5	0.129149E 03	0.170098E-01	0.310000E 01	0.241720E 07
	2.35000000	4624.00000381	95.00000005	
6	0.112345E 03	0.173581E-01	0.235000E 01	0.211028E 07
	2.85000000	4619.50000381	94.00000005	
7	0.123609E 03	0.174547E-01	0.285000E 01	0.233028E 07
	3.12000000	4618.00000381	94.00000005	
8	0.129332E 03	0.169008E-01	0.312000E 01	0.243816E 07
	3.50000000	4615.00000381	94.00000005	
9	0.136982E 03	0.167714E-01	0.350000E 01	0.258237E 07
	3.80000000	4611.00000381	94.50000005	
10	0.142796E 03	0.175419E-01	0.380000E 01	0.268712E 07
	4.40000000	4607.00000381	95.50000005	
11	0.153795E 03	0.169588E-01	0.440000E 01	0.288366E 07
	4.85000000	4603.00000381	96.00000005	
12	0.161541E 03	0.170264E-01	0.485000E 01	0.302345E 07
	5.30000000	4599.00000381	97.00000005	
13	0.169021E 03	0.170825E-01	0.530000E 01	0.315211E 07
	4.20000000	4609.00000381	97.50000005	
14	0.150529E 03	0.168188E-01	0.420000E 01	0.280223E 07
	3.67000000	4612.50000381	97.00000005	
15	0.140648E 03	0.173500E-01	0.367000E 01	0.262298E 07
	3.00000000	4617.00000381	96.00000005	
16	0.127049E 03	0.182401E-01	0.300000E 01	0.237789E 07
	2.00000000	4626.00000381	96.00000005	
17	0.103735E 03	0.184059E-01	0.200000E 01	0.194154E 07
	0.00000000	0.00000000	0.00000000	

4 HARD .0009 40 THIN WITH DUMMY 6-17-70

OSGR	AREA	CBR
4645.50000381	10.00000000	28.75000001

DELP NO.	VEL(FPS)	SGR	CD	TEMP DELP(IN)	REY.NO.
	2.55000000	4614.50000381		93.00000005	
1	0.116817E 03		0.241901E-01	0.255000E 01	0.221024E 07
	2.85000000	4611.00000381		93.00000005	
2	0.123498E 03		0.240875E-01	0.285000E 01	0.233664E 07
	3.20000000	4607.50000381		94.00000005	
3	0.130980E 03		0.236293E-01	0.320000E 01	0.246922E 07
	3.70000000	4602.50000381		94.00000005	
4	0.140841E 03		0.231251E-01	0.370000E 01	0.265513E 07
	4.20000000	4597.00000381		95.00000005	
5	0.150192E 03		0.229778E-01	0.420000E 01	0.282118E 07
	4.60000000	4594.00000381		96.00000005	
6	0.157322E 03		0.222775E-01	0.460000E 01	0.294449E 07
	5.05000000	4587.00000381		97.00000005	
7	0.164986E 03		0.230505E-01	0.505000E 01	0.307686E 07
	5.50000000	4584.50000381		98.00000005	
8	0.172335E 03		0.220691E-01	0.550000E 01	0.320243E 07
	4.65000000	4591.50000381		98.00000005	
9	0.158459E 03		0.231077E-01	0.465000E 01	0.294459E 07
	3.82000000	4602.00000381		98.00000005	
10	0.143623E 03		0.226591E-01	0.382000E 01	0.266889E 07
	3.40000000	4605.50000381		97.50000005	
11	0.135437E 03		0.234098E-01	0.340000E 01	0.252127E 07
	2.45000000	4615.50000381		97.00000005	
12	0.114917E 03		0.243653E-01	0.245000E 01	0.214311E 07
	2.75000000	4613.00000381		96.00000005	
13	0.121640E 03		0.235162E-01	0.275000E 01	0.227666E 07
	3.00000000	4610.50000381		96.00000005	
14	0.127049E 03		0.232147E-01	0.300000E 01	0.237789E 07

	3.30000000	4608.00000381	96.50000005	
15	0.133310E 03	0.226117E-01	0.330000E 01	0.249060E 07
	3.65000000	4603.00000381	97.00000005	
16	0.140265E 03	0.231693E-01	0.365000E 01	0.261583E 07
	4.10000000	4599.50000381	97.00000005	
17	0.148660E 03	0.223250E-01	0.410000E 01	0.277239E 07
	4.69000000	4591.00000381	98.00000005	
18	0.159139E 03	0.231228E-01	0.469000E 01	0.295723E 07
	5.32000000	4584.50000381	99.00000005	
19	0.169643E 03	0.228158E-01	0.532000E 01	0.314119E 07
	4.65000000	4592.00000381	100.00000005	
20	0.158743E 03	0.228938E-01	0.465000E 01	0.292894E 07
	3.61000000	4607.50000381	100.00000005	
21	0.139869E 03	0.209456E-01	0.361000E 01	0.258070E 07
	2.90000000	4611.00000381	99.00000005	
22	0.125250E 03	0.236721E-01	0.290000E 01	0.231920E 07
	2.10000000	4620.00000381	98.00000005	
23	0.106488E 03	0.241623E-01	0.210000E 01	0.197883E 07

1 SOFT 0009 40 THICK WITHOUT DUMMY 6-29-70

OSGR	AREA	CBR
4603.00000381	10.00000000	28.76000000

DELP NO.	VEL(FPS)	SGR CD	TEMP DELP(IN)	REY.NO.
	1.80000000	4590.00000381	88.00000005	
1	0.976847E 02	0.143710E-01	0.180000E 01	0.188246E 07
	1.85000000	4587.50000381	89.00000005	
2	0.991225E 02	0.166716E-01	0.185000E 01	0.190312E 07
	2.35000000	4585.00000381	88.00000005	
3	0.111615E 03	0.152413E-01	0.235000E 01	0.215092E 07

	2.65000000	4581.00000381	89.50000005	
4	0.118688E 03	0.165194E-01	0.265000E 01	0.227458E 07
	2.75000000	4581.50000381	89.00000005	
5	0.120851E 03	0.155569E-01	0.275000E 01	0.232031E 07
	3.30000000	4575.25000381	90.50000005	
6	0.132567E 03	0.167327E-01	0.330000E 01	0.253124E 07
	4.12000000	4570.25000381	91.50000005	
7	0.148259E 03	0.158172E-01	0.412000E 01	0.282051E 07
	4.52000000	4568.00000381	93.00000005	
8	0.155500E 03	0.154080E-01	0.452000E 01	0.294214E 07
	4.93000000	4564.00000381	94.00000005	
9	0.162546E 03	0.157411E-01	0.493000E 01	0.306431E 07
	5.65000000	4557.50000381	95.00000005	
10	0.174169E 03	0.160243E-01	0.565000E 01	0.327156E 07
	4.43000000	4569.50000381	95.50000005	
11	0.154292E 03	0.150473E-01	0.443000E 01	0.289297E 07
	3.70000000	4574.75000381	95.00000005	
12	0.140944E 03	0.151926E-01	0.370000E 01	0.264747E 07
	2.71000000	4584.00000381	95.00000005	
13	0.120623E 03	0.139508E-01	0.271000E 01	0.226577E 07
	2.00000000	4590.00000381	94.00000005	
14	0.103530E 03	0.129339E-01	0.200000E 01	0.195175E 07
	2.58000000	4585.00000381	94.00000005	
15	0.117588E 03	0.138825E-01	0.258000E 01	0.221676E 07
	3.28000000	4579.00000381	93.50000005	
16	0.132524E 03	0.145597E-01	0.328000E 01	0.250287E 07
	3.90000000	4573.00000381	94.00000005	
17	0.144573E 03	0.153064E-01	0.390000E 01	0.272547E 07
	4.55000000	4568.50000381	95.00000005	
18	0.156297E 03	0.150877E-01	0.455000E 01	0.293587E 07
	6.00000000	4555.00000381	97.00000005	
19	0.179805E 03	0.159186E-01	0.600000E 01	0.335323E 07
	4.47000000	4569.00000381	97.00000005	
20	0.155196E 03	0.151352E-01	0.447000E 01	0.289428E 07
	3.61000000	4575.25000381	97.00000005	

```
 21   0.139470E 03    0.152958E-01    0.361000E 01    0.260100E 07
    2.61000000  4584.50000381     96.50000005
 22   0.118536E 03    0.141042E-01    0.261000E 01    0.221458E 07
    2.05000000  4588.50000381     96.00000005
 23   0.105006E 03    0.140744E-01    0.205000E 01    0.196532E 07
    0.00000000     0.00000000     0.00000000


 2      SOFT 0009 40 THICK WITH DUMMY 6-29-70

OSGR            AREA            CBR
 4602.00000381     10.00000000     28.76000000
DELP            SGR             TEMP
NO.      VEL(FPS)          CD            DELP(IN)        REY.NO.

    1.80000000  4580.50000381     92.00000005
  1   0.980406E 02    0.237674E-01    0.180000E 01    0.186174E 07
    2.85000000  4569.50000381     92.00000005
  2   0.123365E 03    0.226911E-01    0.285000E 01    0.234264E 07
    3.38000000  4564.00000381     93.00000005
  3   0.134468E 03    0.223709E-01    0.338000E 01    0.254420E 07
    4.15000000  4556.00000381     93.50000005
  4   0.149067E 03    0.220560E-01    0.415000E 01    0.281530E 07
    4.60000000  4550.50000381     95.00000005
  5   0.157154E 03    0.222775E-01    0.460000E 01    0.295195E 07
    5.25000000  4544.00000381     96.00000005
  6   0.168041E 03    0.219829E-01    0.525000E 01    0.314511E 07
    5.75000000  4538.00000381     97.00000005
  7   0.176019E 03    0.221477E-01    0.575000E 01    0.328262E 07
    4.72000000  4550.25000381     97.00000005
  8   0.159477E 03    0.218165E-01    0.472000E 01    0.297412E 07
    4.10000000  4558.50000381     97.50000005
  9   0.148701E 03    0.211116E-01    0.410000E 01    0.276819E 07
    3.52000000  4565.00000381     97.50000005
 10   0.137782E 03    0.209159E-01    0.352000E 01    0.256493E 07
```

	3.00000000	4570.00000381	97.00000005		
11	0.127141E 03	0.212249E-01	0.300000E 01	0.237109E 07	
	1.85000000	4585.00000381	97.00000005		
12	0.998421E 02	0.182849E-01	0.185000E 01	0.186197E 07	
	2.25000000	4578.00000381	96.50000005		
13	0.110058E 03	0.212249E-01	0.225000E 01	0.205618E 07	
	3.02000000	4570.00000381	96.00000005		
14	0.127450E 03	0.210843E-01	0.302000E 01	0.238539E 07	
	3.45000000	4565.25000381	96.00000005		
15	0.136221E 03	0.211960E-01	0.345000E 01	0.254956E 07	
	3.99000000	4559.00000381	97.00000005		
16	0.146627E 03	0.214443E-01	0.399000E 01	0.273447E 07	
	4.88000000	4548.00000381	97.50000005		
17	0.162230E 03	0.220186E-01	0.488000E 01	0.302005E 07	
	5.65000000	4539.00000381	98.50000005		
18	0.174717E 03	0.221875E-01	0.565000E 01	0.324091E 07	
	4.64000000	4550.25000381	99.00000005		
19	0.158403E 03	0.221926E-01	0.464000E 01	0.293307E 07	
	3.90000000	4560.00000381	99.00000005		
20	0.145224E 03	0.214290E-01	0.390000E 01	0.268903E 07	
	3.30000000	4567.00000381	98.00000005		
21	0.133467E 03	0.211043E-01	0.330000E 01	0.248016E 07	
	2.20000000	4579.00000381	97.00000005		
22	0.108877E 03	0.208028E-01	0.220000E 01	0.203048E 07	
	1.65000000	4587.00000381	97.50000005		
23	0.943332E 02	0.180894E-01	0.165000E 01	0.175609E 07	
	0.00000000	0.00000000	0.00000000		

3 HARD 0009 40 THICK WITHOUT DUMMY 7-13-70

OSGR	AREA	CBR
4571.00000381	10.00000000	28.78000000

DELP NO.	SGR VEL(FPS)	CD	TEMP DELP(IN)	REY.NO.

```
   3.72000000  4542.50000381     92.50000005
 1   0.140957E 03   0.152447E-01   0.372000E 01   0.267183E 07
   4.40000000  4538.00000381     93.00000005
 2   0.153369E 03   0.149237E-01   0.440000E 01   0.290181E 07
   4.98000000  4534.70000267     94.00000005
 3   0.163312E 03   0.145042E-01   0.498000E 01   0.307874E 07
   5.55000000  4530.00000381     95.50000005
 4   0.172638E 03   0.146996E-01   0.555000E 01   0.323697E 07
   4.48000000  4538.00000381     96.50000005
 5   0.155246E 03   0.146572E-01   0.448000E 01   0.290041E 07
   3.67000000  4544.50000381     96.00000005
 6   0.140449E 03   0.143680E-01   0.367000E 01   0.262868E 07
   2.45000000  4554.00000381     95.50000005
 7   0.114702E 03   0.138070E-01   0.245000E 01   0.215067E 07
   1.60000000  4559.00000381     95.00000005
 8   0.926522E 02   0.149237E-01   0.160000E 01   0.174036E 07
   0.00000000     0.00000000     0.00000000
```

100

```
 4     HARD 0009 40 THICK WITH DUMMY 7-13-70

OSGR            AREA            CBR
 4569.00000381     10.00000000     28.78000000
DELP            SGR             TEMP
NO.      VEL(FPS)          CD           DELP(IN)        REY.NO.

   2.15000000  4548.00000381     89.00000005
 1   0.106820E 03   0.194356E-01   0.215000E 01   0.205092E 07
   2.96000000  4545.20000267     89.50000005
 2   0.125394E 03   0.159993E-01   0.296000E 01   0.240310E 07
   3.52000000  4535.20000267     90.00000005
 3   0.136805E 03   0.191069E-01   0.352000E 01   0.261696E 07
   4.13000000  4530.00000381     91.00000005
 4   0.148320E 03   0.187902E-01   0.413000E 01   0.282684E 07
```

```
    4.70000000  4524.50000381     92.00000005
 5   0.158368E 03   0.188399E-01   0.470000E 01   0.300733E 07
    5.22000000  4519.00000381     93.00000005
 6   0.167050E 03   0.190597E-01   0.522000E 01   0.316066E 07
    5.72000000  4514.50000381     94.00000005
 7   0.175025E 03   0.189591E-01   0.572000E 01   0.329957E 07
    4.70000000  4524.50000381     94.00000005
 8   0.158654E 03   0.188399E-01   0.470000E 01   0.299094E 07
    3.80000000  4532.00000381     94.00000005
 9   0.142657E 03   0.193747E-01   0.380000E 01   0.268937E 07
    2.92000000  4540.50000381     93.50000005
10   0.124996E 03   0.194213E-01   0.292000E 01   0.236070E 07
    2.10000000  4550.00000381     93.00000005
11   0.105955E 03   0.180032E-01   0.210000E 01   0.200471E 07
    2.92000000  4540.50000381     93.00000005
12   0.124940E 03   0.194213E-01   0.292000E 01   0.236393E 07
    3.47000000  4536.50000381     92.50000005
13   0.136138E 03   0.186368E-01   0.347000E 01   0.258048E 07
    4.11000000  4530.00000381     93.00000005
14   0.148228E 03   0.188816E-01   0.411000E 01   0.280455E 07
    4.35000000  4522.50000381     94.00000005
15   0.152633E 03   0.212706E-01   0.435000E 01   0.287742E 07
    5.60000000  4515.20000267     95.00000005
16   0.173336E 03   0.191166E-01   0.560000E 01   0.325592E 07
    4.20000000  4529.70000267     95.00000005
17   0.150113E 03   0.186191E-01   0.420000E 01   0.281971E 07
    3.18000000  4539.50000381     95.00000005
18   0.130619E 03   0.184591E-01   0.318000E 01   0.245354E 07
    1.75000000  4552.50000381     94.00000005
19   0.968106E 02   0.187613E-01   0.175000E 01   0.182506E 07
  -0.01000000     0.00000000     0.00000000
```